Extrusive upper crust formation at slow-spreading ridges: Fault steering of lava flows

C. Gini, Javier Escartin, M. Cannat, T. Barreyre

Extrusive upper crust formation at slow-spreading ridges: fault steering of lava flows

C. Gini[1,3,*], J. Escartín[2], M. Cannat[3] & T. Barreyre[4]

[1]Dept. of Earth Sciences, Memorial University of Newfoundland, St. John's, Canada

[2]Laboratoire de Géologie, UMR 8538, Ecole Normale Supérieure, PSL Research University, CNRS, Paris, France

[3]Université de Paris, Institut de Physique du Globe de Paris, UMR 7154, CNRS, Paris, France

[4]Centre for Deep Sea Research, University Bergen, Bergen, Norway

***Corresponding author:** cgini@mun.ca. Now at Memorial University of Newfoundland, St John's, Canada.

Citation:
C. Gini, J. Escartín, M. Cannat, T. Barreyre, 2021, Extrusive upper crust formation at slow-spreading ridges: Fault steering of lava flows, Earth and Planetary Science Letters, V. 576, 117202, https://doi.org/10.1016/j.epsl.2021.117202.

Abstract

The structure of the oceanic upper volcanic crust is less understood at slow-spreading ridges than at faster ones. Its construction is dominated by pillow lavas, reflecting lower effusion rates than those at fast spreading ridges, where sheet and lobate flows are common and flow off-axis while thickening the extrusive volcanic layer. Based on optical and high-resolution bathymetry data from the Lucky Strike segment (Mid-Atlantic Ridge), we document a mode of volcanic emplacement that likely operates at some magmatically robust slow- and ultra-slow spreading ridge segments, in the presence of strong gradients in magma supply. In these settings, sheet flows may efficiently transport melt away from magmatically robust segment centers in the along-axis direction, steered by normal faults, and exploiting along-axis topographic gradients, with limited across-axis flow. Surface lineations of sheet lava flows tend to be subparallel to fault scarps and the overall segment orientation, and show whorls, well-developed lava channels with associated levees, and surface fold structures at flow fronts. This mode of lava emplacement transitions away from the segment center to pillow-dominated seafloor near the segment ends, associated often with hummocks and axial volcanic ridges. This results in local lava emplacement due to a melt supply that is lower than at the segment center. We propose that fault-steering of lava flows along-axis, limiting off-axis transport as observed at fast-spreading systems, may be common at both slow- and ultra-slow spreading ridges with significant along-axis changes in magma supply linked to topographic gradients. As a result, the nature and properties of the extrusive volcanic

layer may vary significantly along axis owing to changes in the modes of volcanic emplacement, as transitions from sheet flows to pillow lavas may impact the porosity structure and hence the seismic properties of the extrusive layer in the oceanic upper crust.

Keywords: *Mid-ocean ridges; faulting; submarine volcanism; lava flows; morphology.*

Highlights

- Faults steer sheet flows over a few km along axis, impacting upper crust construction
- Along-axis changes in lava flow morphologies, evidence for melt supply gradients
- Different lava flow morphologies may affect seismic properties of Layer 2A

1. Introduction

Volcanic emplacement at the axis of mid-ocean ridges determines the nature, geometry and physical properties of the uppermost extrusive volcanic layer of the oceanic crust. Constraints on this structure have been obtained from geological observations (e.g., submersible studies and ophiolites), and from drilling. At fast-spreading ridges, the volcanic layer is built through surface eruptions emanating from the axial summit trough, lava flows extending off-axis, in addition to dikes that do not reach the surface (Fornari, 1986; Hooft et al., 1996; Soule et al., 2009). Slow-spreading ridges display a wide variety of volcanic morphologies resulting from varying melt supply both at the scale of individual ridge segments and regionally. Based on seafloor observations, it has been

53 suggested that pillow lavas are ubiquitous and often emanating from hummocks, small
54 seamounts, or axial volcanic ridges, (Smith and Cann, 1992; Smith and Cann, 1993; Searle
55 et al., 2010; Yeo et al., 2012; Estep et al., 2019), dominating upper crustal construction at
56 slow spreading ridges (see also Figure S6 of Chen et al., 2021). Pillow lavas also suggest
57 flow rates and lateral lava transport that are limited relative to sheeted lava flows (e.g.,
58 Griffiths and Fink, 1992; Gregg and Fink, 1995). Sheet flows, which are common at fast
59 spreading ridges, are scarce at slow- and ultra-slow spreading ridges (see Figure S6 in
60 Chen et al., 2021), but they have been reported primarily at large seamounts or central
61 volcanoes (Atwater; 1979; Gracia et al., 1998; Bideau et al., 1998; Bonatti and Harrison,
62 1988; Edwards et al., 2001; Deschamps et al., 2007; Escartín et al., 2014; Asada et al., 2015),
63 and therefore in areas where magma supply and hence eruption rates are likely elevated.
64 These studies do not report neither the geometry nor the extent and direction of these
65 sheet flows.

66 At fast spreading ridges, seismic Layer 2A, interpreted to represent the extrusive upper
67 crust, is thinnest at the axis (~200 m) and thickens away from it (Kent et al., 1994; Hooft
68 et al., 1996). At slow spreading ridges, seismic Layer 2A may be completely absent along
69 magmatically-starved ridge sections, such as the South-West Indian Ridge (Sauter et al.,
70 2013), or its thickness may exceed that of fast-spreading ridges, being up to 500 m thick
71 or more at magmatically robust crustal sections (e.g., Hussenoeder et al., 2002; Seher et
72 al., 2010c). Hence, the geometry, nature, and mode of emplacement of the extrusive upper

crust at slow-spreading ridge sections is both more variable and complex than that of fast-spreading ridges.

Seismic studies at on-axis Atlantic oceanic crust yield Layer 2A thicknesses that typically vary between 350-500 m (Hussenoeder et al., 2002; Peirce et al., 2007; Seher et al., 2010c) and may reach up to 850 m (Arnulf et al., 2014), with thicknesses up to ~1000 m off-axis (Estep et al., 2019). The overall seismic velocity of Layer 2A, as well as its vertical gradient, also show a temporal evolution attributed to hydrothermal alteration or clogging, pore geometry changes, among other factors (e.g., Wilkens et al., 1991; Grevemeyer et al, 1999; Estep et al., 2019). Layer 2A thickness variations of a few hundreds of m over spatial scales of ~10-20 km are also well-documented (e.g., Peirce et al., 2007; Seher et al., 2010c; Estep et al., 2019). At the Lucky Strike segment, Layer 2A thickness and upper crust velocity variations have been attributed primarily to a tectonically induced porosity reduction towards the segment ends (Crawford et al., 2010; Seher et al., 1010c), while in other studies and sites variations in seismic properties are attributed to alteration, volcanism, and to interactions among various processes (e.g., Christeson et al., 2019, and references therein).

The Lucky Strike segment is an ideal site to study links between volcanic style (e.g., sheet, lobate and pillow lava flows), and melt supply gradients along the segment, that may be linked to effusion rates (e.g., Griffiths and Fink, 1992; Gregg and Fink, 1995). We analyze high-resolution bathymetry and seafloor imagery, acquired with deep-sea vehicles over several cruises, to quantify the relative importance and along-axis variations of lava

94 morphologies, and document directions of surface lava transport, coupled to geophysical
95 data available from the area (shipboard multibeam bathymetry, sonar, and prior seismic
96 reflection studies). We propose a conceptual model of lava emplacement at magmatically
97 robust slow-spreading ridge segments, that takes into account variations in eruption rate
98 and lava transport along-axis. This model is fundamentally different from that proposed
99 for fast-spreading ridges, and has consequences for both the overall structure of the upper
100 volcanic layer, its physical properties (i.e., porosity and thus seismic Layer 2A structure),
101 and its possible variations along-axis linked to melt supply changes that are common at
102 magmatically robust slow-spreading ridge segments. The observations at Lucky Strike
103 that we report here, likely apply to numerous magmatically robust slow- and ultra-slow
104 spreading segments which show either elevated central areas, or central volcanos similar
105 to those at Lucky Strike (e.g., Escartín et al., 2014). This is also supported by the
106 observation of sheet flows at the center of several segments along the Mid-Atlantic Ridge
107 (e.g., Atwater; 1979; Stakes et al., 1984; Gracia et al., 1998) and other slow-spreading
108 ridges (e.g., Asada et al., 2015).

109 **2. Geological Setting**

110 The ~70 km long Lucky Strike ridge segment of the Mid-Atlantic Ridge (MAR) at
111 ~37.25°N (Figure 1) is magmatically robust, and influenced by the nearby Azores hotspot
112 to the Northeast (Cannat et al., 1999). Off axis, the older crust shows well-developed
113 ridge-parallel, fault-bounded abyssal hills. At the segment center, a ~20 km diameter
114 central volcano is underlain by a magma chamber at ~3 km depth beneath the seafloor

115 (Singh et al., 2006; Escartín et al., 2014), hosting at its summit one of the largest deep-sea
116 hydrothermal fields along the MAR (Figure 2b *h* and *v*; Langmuir et al., 1997; Humphris
117 et al., 2002; Ondréas et al., 2009; Barreyre et al., 2012; Escartín et al., 2014). The rift valley
118 floor deepens along axis from ~1700 m depth at the central volcano summit, to >4000 m
119 at the segment ends (nodal basins), while the axial valley transitions from a narrow, <2
120 km wide rift zone that dissects the volcano summit (V1 and V2 in Figure 2b), to a broad
121 valley floor at the segment ends. The rift valley lacks axial volcanic ridges in its shallowest
122 section (Figure 2a and b), but these are common at distances >10 km from the segment
123 center (Figure 2c and d, and south of *t* in 2b).

124 Previous geophysical studies along this segment provide bathymetry, gravity, seismic
125 reflection and refraction data (Cannat et al., 1999; Singh et al., 2006; Seher et al., 2010a;
126 Seher et al., 2010b; Seher et al., 2010c; Crawford et al., 2010; Combier et al., 2015).
127 Geophysical data indicate that the crustal thickness is ~7-8 km at the segment center, and
128 thins to <4 km at its ends (Detrick et al., 1995; Cannat et al., 2008; Crawford et al., 2010;
129 Seher et al., 2010c), likely due to magma being focused to the segment center, and with
130 reduced melt supply to the segment ends (Detrick et al., 1995). Fault patterns also change
131 along-axis, while the rift widens and deepens towards the segment ends (e.g., Cannat et
132 al., 1999; Escartín et al., 2014). Seismic data shows a clear Layer 2A/2B boundary at a two-
133 way travel time of 0.4-0.5 s below seafloor (Singh et al., 2006; Seher et al., 2010c) and that
134 corresponds to a thickness of >600 m (see discussion in Section 7.2).

135 **3. Data and surveys**

We benefit from data previously acquired at the Lucky Strike segment during several cruises over more than 20 years. Here we summarize the datasets used, while full information is provided both in the Supplementary Materials and in the references. Shipboard multibeam bathymetry data, gridded at 40 m and fully covering the ridge segment and adjacent crust, were acquired during the SISMOMAR (https://doi.org/10.17600/5010040) and SUDAÇORES (https://doi.org/10.17600/98010080) cruises (Figure 1a). High-resolution sidescan sonar data, covering the central part of the rift valley floor (Figure 1b), were acquired with the deep-towed WHOI DSL120 system during the Lustre'96 cruise (http://www.marine-geo.org/tools/entry/KN145-19). Sonar grids are publicly available (Data DOI: 10.1594/IEDA/321460) and processing details are given in Escartín et al. (2014). Near-bottom multibeam bathymetry data (Figure 1b) were acquired during 3 cruises: MOMARETO 2006 (https://doi.org/10.17600/6030130), MOMAR'08-Leg 1 (https://doi.org/10.17600/8010140) and BATHYLUCK'09 (https://doi.org/10.13155/47147). Those surveys were conducted using both the remotely operated vehicle (ROV) VICTOR and the autonomous underwater vehicle (AUV) AsterX. The high-resolution bathymetry grids in Figure 1b are publicly available (https://doi.org/10.17882/80574).

Seafloor images were obtained from a) Vertical electronic still images acquired with the WHOI TowCam System (GRAVILUCK'06 cruise, https://doi.org/10.17600/6010110), along several profiles crossing the ridge axis and distributed along-axis; b) Submersible

157 Nautile video images (Figure 1a; GRAVILUCK'06 cruise), primarily along the ridge axis;
158 c) ROV VICTOR video imagery (Figure 1a; MOMAR2008 and BATHYLUCK'09 cruises,
159 respectively https://doi.org/10.17600/8010110 and https://doi.org/10.17600/9030040)
160 both along the axis and in adjacent areas; and d) seafloor photomosaics over the Lucky
161 Strike hydrothermal field (Figure 1a; Barreyre et al., 2012), derived from processed black-
162 and-white vertical images acquired with ROV VICTOR (MOMAR2008 and
163 Bathyluck'09), and publicly available (https://doi.org/10.17882/77449,
164 https://doi.org/10.17882/77405). Photomosaics from ROV surveys (outlines shown in
165 Figure 2a), and from individual camera tows, are also publicly available (see
166 Supplementary materials for details).

167 **4. Identifying volcanic features to constrain volcanic style**

168 To document and quantify the variations in volcanic style along-axis, we integrate the
169 interpretation of both high-resolution bathymetry, and optical seafloor imagery (Figures
170 1 to 4), that also cover a wide range of spatial scales (from ~1 km, Figures 2 and 3, to <1
171 m, Figure 4). Bathymetry, coupled with available sonar imagery (see Escartín et al., 2014)
172 is primarily used to identify volcanic structures at larger scales, such as the limits and
173 structure of lava flows, volcanic ridges, collapse pits associated with fissures, in addition
174 to faults and fissures that are pervasive in the area (Figure 2). Imagery is used to quantify
175 the distribution and abundance of dominant volcanic style along camera tow transects
176 and on photomosaics (Figures 1, 2 and 4). As seafloor optical imagery is also oriented and

177 scaled, we digitize the orientation of lava flow structures (e.g., lineations on lava flow
178 surfaces) to determine the direction of lava flow transport in the study area.

179 The bathymetry shows a clear gradient in fine-scale seafloor morphology away from the
180 Lucky Strike segment center. At and around the central Lucky Strike volcano, that shows
181 summital volcanic cones (V1 and V2 in Figure 2), the smooth volcanic seafloor is faulted
182 by a dense network of closely spaced normal faults that bound numerous horsts and
183 grabens (Figure 2a and b). South of the volcanic cone V2 (Figure 2), this smooth volcanic
184 seafloor transitions to hummocky seafloor, typical of slow-spreading ridges, at a distance
185 of ~2.5 km in the along-axis direction (Figures 2 and 3; Escartín et al., 2014), with well-
186 developed axial volcanic ridges further south (Figures 1 and 2). The seafloor relief also
187 reveals the recent, mostly unfaulted along-axis lava flow (Figure 2).

188 Based on seafloor imagery, we identify and map systematically the distribution of
189 different lava morphologies: sheet flows, lobate flows, and pillows throughout the study
190 area (Figures 2, 3 and 4). In addition to quantifying along-axis variations in the mode of
191 lava flow emplacement, we also a) document the structure of the most recent axial lava
192 channels (Figures 2, 4a, 5), b) determine if the sheet flows are sedimented or
193 unsedimented as a proxy of age, c) study the nature of collapse pits along fissures and
194 grabens (Figure 2) and d) digitize lineations on the sheet flow surface to document the
195 flow direction and the patterns of associated surface melt transport (Figure 6).

196 ***4.1 Along-axis lava flows and faulting***

The high-resolution bathymetry in Figures 2 and 3 reveals a young 3-km long sheet flow, which originated at the base of the unrifted southern volcanic cone V2 in Figure 2 at the summit of the central volcano. This lava flow is the youngest identified in the area, it is unfaulted, displays an acoustically reflective surface (Fig. 6 in Escartín et al., 2014), and seafloor observations show that it is visually fresh and unsedimented lavas (Figure 4 a and b; Escartín et al. 2015). The across-flow profiles (Figure 5b) show a ~150 m wide channel near its source, with a central part that is lower at the center relative to its edges (1-4 m, p1 in Figure 5b). Distal parts of the flow show instead a domed structure, with a lava flow center higher by a few m (e.g., p2, p4, p6 in Fig. 5b) to >10 m (e.g., p5) with respect to the flow margins. This lava flow was clearly steered by normal fault scarps (Figure 3a and 5b) and exploited mild topographic gradients that increase from ~1.2° near the volcanic cone to ~5.2° further to the south (Figure 5).

The high-resolution bathymetry and seafloor imagery reveal older sheet flows both in the central area (Figures 3a and 4c) or emplaced in low areas among hummocks downrift from the segment center (Figures 2 and 3c). In all cases, the main flow direction appears to be along-axis, and steered by either axis-parallel faults or the flanks of hummocky ridges, which also tend to be elongated along-axis. These sheet flows show a folded surface morphology, with an amplitude of 1-2 m, and wavelengths of ~10-20 m in along-flow profiles (Figure 5c). Locally, these structures show evidence of flow off-axis instead of along-axis, that have breached laterally at fault terminations, or covered and flowed over faults (Figure 3). On camera tow imagery, older sheet flows can be identified when

lineations or whorls are apparent through the thin sediment veneer covering them (Figure 4c).

Near the young sheet flow source, the depressed flow center shows surface lineations and whorls, that vary in size from a few m to up to ~20 m in diameter (Figure 4a). Striated lava surfaces within lava flow channels are common along many ridge sections (e.g., East Pacific Rise; Chadwick et al., 1999) and their orientation indicate the lava flow direction. The lineations that we observe at Lucky Strike also seem to be reliable indicators of lava transport; they are visible in photomosaics over lava flows that are well constrained on the bathymetry (Figure 2a and 4), and their distribution could also be observed in detail during a submersible dive following this recent lava flow (see Figure 1a and 4b). These textures (Figure 4) document both high effusion rates and shearing of the lava flow surface during its emplacement (Ballard et al., 1979; Griffith and Fink, 1992; Gregg and Fink, 1995; Lonsdale, 1977). Flow margins that are raised relative to the flow center have hackly lavas that record the break-up of the lava surface at flow edges (Figure 4a; Chadwick et al., 1999; Soule et al., 2005). These volcanic facies are similar to those from lava channels at the EPR, that also show a depressed lava channel likely recording drainage downflow away from the axis during lava emplacement and subsequent deflation (e.g., Chadwick, 2003; Soule et al., 2005).

Recent lava flows erupted at Lucky Strike segment center have thus been efficiently steered along-axis by normal fault scarps, and also along the flanks of hummocky ridges, which are aligned along-axis, following gentle along-axis topographic gradients. Lava

239 flows can breach laterally and flow short distances off-axis, particularly in areas of low
240 fault scarp relief (for example at ~37.27°N in Figure 3a).

241 ***4.2 Lobate and pillow lavas***

242 Our imagery reveals that both lobate and pillow lavas (Figure 4 d and e) are present
243 throughout the study area. Lobate lava morphology, which corresponds to local flow
244 rates intermediate between those of sheet flows and pillow lavas (e.g., Griffiths and Fink,
245 1992), are commonly found at the edges of sheet flows or preserved between branches of
246 jumbled flow. Pillow lavas are found throughout, and particularly making up hummocks
247 and axial volcanic ridges. In sloping areas, pillows are elongated, indicating the direction
248 of lava transport downslope (Figure 4e). Both hummocks and axial volcanic ridges thus
249 build up through pillow lava emplacement as observed elsewhere along the MAR (e.g.,
250 Ballard et al., 1975; Yeo et al., 2012).

251 ***4.3 Grabens and collapses***

252 The high-resolution bathymetry also reveals faults and narrow grabens (10-50 m wide
253 and up to 15-20 m deep), that are both parallel and oblique to the ridge axis (Figure 3).
254 Collapse pits, with circular or elongated shapes are clearly aligned along some faults
255 forming narrow grabens (Figure 3a and 4f), that are likely associated with dikes
256 subseafloor subparallel to the ridge axis. Pit diameter is variable and ranges from a few
257 m, to structures that are wider than 50 m, and with depths reaching ~20 m. Imagery and
258 high-resolution bathymetry data show that the edges of these pits lack both elevated rims

and debris, features expected for structures of an explosive origin (volcanic degassing or hydrothermal explosions). Instead, the morphology is consistent with local gravity collapse, and comparable collapse features associated with dike-induced grabens have been identified both in subaerial volcanic environments (e.g., Okubo and Martel, 1988) and at other planets albeit at much larger scales (e.g., Mege et al., 2003; Davey et al., 2012). Some pits are flat-bottomed, a structure that is consistent with possible lava infill linked to underlying diking along pitted fissures and grabens. Other pits show instead a concave morphology consistent with debris infill due to gravity collapse with no lava infill.

5. Along-axis lava transport by sheet flows

High-effusion rate submarine eruptions feed lava flows that follow topographic gradients, transporting lava downslope over distances of hundreds of m to a few km (e.g., Gregg and Fornari, 1998). The flow front stops advancing either when lava effusion ceases at the source (volume-limited eruptions) or when lava is efficiently cooled, and the solidification of the crust stops the flow (cooling-limited eruption), as is the case at very short spatial scales (meters) for pillow lavas (e.g., Griffiths and Fink, 1992; Gregg and Fink, 1995; Gregg et al., 1998). Sheet flow lava morphology is thus indicative of relatively high eruption rates, significant eruptive volumes, or both (e.g., Griffiths and Fink, 1992; Gregg and Fink, 1995). This is consistent with the presence of lava whorls (Figure 4 a and c) and well-developed lava channels near the source of the young lava flow (Figures 3 and 4) that emanates from the base of the volcanic cone (V2 in Figure 2) at the summit of the central volcano, and that shows incipient rifting (Escartín et al., 2015).

280 The most recent flows identified here flowed southwards (Figure 3), as shown by surface
281 folding away from the lava source (Figure 5c), and by the orientation of lineated lavas,
282 that clearly indicate lava transport direction (e.g., Chadwick et al., 1999). Both the
283 bathymetry and the fault-parallel lineations demonstrate that they are topographically
284 constrained and emplaced against fault scarps, typically <10 m in height (Figure 5).
285 Based on the imagery throughout the study area (TowCam tracks and photomosaics,
286 Figures 1, 2 and 4) sheet flows in general show orientation centered at ~5-15° NE (Figure
287 6b), consistent with that of fault traces identified in high-resolution sonar data (Escartín
288 et al., 2014) and with the overall orientation of the Lucky Strike ridge segment (~18° and
289 ~19° NE respectively). This agreement suggests widespread lava steering by faults at the
290 center of this segment over at least the last few tens of thousands of years, corresponding
291 to the expected time span required to construct the seafloor in the study area. On Figure
292 6b, the sheet flow lineation orientations along TowCam tracks display more variation
293 than those from lava flows imaged by the photomosaics. This can be the result of local
294 variations in the flow direction within lava flows, which typically flow subparallel to the
295 ridge axis and faults, but instead flow off-axis, in directions oblique to sub-perpendicular
296 to faults, such as those breaching faults and that are visible in the bathymetry (Fig. 3a).

297 While it is not possible to know pre-lava topography in this area, the high-resolution
298 bathymetry constrains a range of plausible thickness along the axial lava flow. Based on
299 the across-axis profiles, we estimate that the thickness of the youngest on-axis flow may
300 vary between a minimum of ~2 m, and a maximum of ~10 m (profiles *p3* and *p5* in Figure

5b). With an average width of 50-75 m and a total length of ~2500 m (Figure 2a), we estimate minimum and maximum lava flow volumes of ~0.25 and 1.9 x 10^6 m^3. For comparison, these volumes are 1 to 2 orders of magnitude lower than the 2005-2006 axial eruption at 9°N along the EPR (Soule et al., 2007), or than other documented eruptions along the EPR, Juan de Fuca, and Gorda Ridges (Clague et al., 2017; see also compilation by Gregg and Fornari, 1998).

6. Along-axis variations in mode of lava emplacement

Seafloor imagery acquired on- and across-axis documents both the relative abundance of different lava morphologies, and their variation along-axis (Figures 1 and 6a). Sheet flows are the dominant mode of lava emplacement at the center of the study area, accounting for ~35% of characterized seafloor, locally exceeding >40% (Figure 6a). At the northern and southern ends of the segment, in contrast, sheet flows account for only ~10-20% of identified seafloor textures, while pillow lavas are most abundant (>40%; Figure 6a). Lobate flows, representing effusion rates intermediate between those of sheet flows and pillows, are present throughout, but are less abundant (~20% or less), and show no systematic along-axis variation (Figure 6a).

The towed camera photographed sedimented seafloor off-axis (Figure 6a), where the morphology of the underlying seafloor cannot be determined unequivocally. Fissures in these sedimented areas may reveal the underlying volcanic seafloor, under a thin sediment veneer (see supplementary material Figure S1b). In most cases the sediment

cover is thin, and efficiently covers flat sheet flows, while it cannot fully cover pillows and lobate lavas. This suggests that completely sedimented areas are likely sheet flows with a thin sedimented veneer, and therefore the relative abundance of sheet flows may be somewhat higher than indicated by the positively identified lava textures, particularly at the center of the segment (Figure 6a, S1b).

While the overall abundance of sheet flows increases towards the segment center, tracks CT09 and CT05 in Figure 6a, across the summit of the central volcano, show a local decrease in the abundance of sheet flows instead. The summit of the central volcano shows a complex recent history of volcanic emplacement that includes two volcanic cones (V1 and V2 in Figure 2) at two different stages of rifting (e.g., Escartín et al., 2015), leading to the formation of a depression hosting a fossil lava lake (Ondréas et al., 2009). These volcanic cones are built up by local lava emplacement dominated by pillows, but also sourcing and feeding the sheet flows which emanated from their base (Figure 2 and 3).

7. Discussion

7.1 Sheet flows and along-axis fault steering of lava flows at slow-spreading ridges

The eruption of pillow lavas which build both hummocks and axial volcanic ridges, is considered to be the main mechanism of upper volcanic crust construction at slow-spreading mid-ocean ridges. Our results suggest that along segments that are both magmatically robust and with associated along-axis variations in melt supply to the seafloor, this upper volcanic crust construction may be locally controlled by the

interaction of faults that steer lava flows along the ridge axis. This is also consistent with geological observations at the several magmatic ridge segments, particularly along the MAR (e.g., Ballard et al., 1979; Atwater 1979; Crane and Ballard, 1981; Gracia et al., 1998; Stakes et al., 1984), that report sheet flows at their segment centers reflecting focusing of melt, and enhanced delivery of lava to the seafloor, at these locations (e.g., Atwater, 1979; Gracia et al., 1998; Bideau et al., 1998).

The sheet flow abundance that we determine optically (~30-40% at the segment center, Figure 6) is much higher than that reported for some slow-spreading sites (e.g., 10-15% at the AMAR segment, Atwater, 1979; or ~10% at the Marianas 17°S segment, Asada et al., 2015) or fast ones (20% at EPR at 9°50'N, Kurras et al., 2000) and commensurable to the abundances reported along other areas of the EPR (~30-50%, White et al., 2002) or at Axial Caldera along the Juan de Fuca Ridge (~40%, Embley et al., 1990), sites that are extremely active magmatically. While there is no information on the orientation of lineated flows at other slow-spreading ridges, these sheet flows are commonly reported in low-lying areas at the feet of axial volcanic ridges and fault scarps (e.g., Stakes et al., 1984), as it is the case for the Lucky Strike flows (Figure 2).

Along-axis fault-control on the mode of lava emplacement at Lucky Strike is also consistent with a recent lava eruption identified along the Reykjanes Ridge (Crane et al., 1997), that is emplaced along a system of faults defining a graben, and that extends ~3 km along-axis, a similar length to that of the axial flow at Lucky Strike (Figure 3a). This type of fault-controlled lava flow is also observed in terrestrial rift systems, mainly in the

AFAR area and along the East African Rift (Figure 7). As in the case of Lucky Strike and other slow- and ultra-slow volcanic ridge segments, volcanoes often develop at the center of rift zones, and are densely dissected by parallel fissures, faults, and grabens (e.g., Dumont et al., 2019). For example, the recent lava flow SE of Hayli Gub volcano, shown in Figure 7a, flowed >15 km along the center of the axial graben (Barberi and Varet, 1971), while the several flows along the Dabbahu-Manda Hararo rift extend >10 km, also along-graben (Figure 7b). The interaction of lava flows with fault scarps, that is also observed at the East Pacific Rise (e.g., Escartín et al., 2007), probably results in the partial or complete burial of some tectonic features, and results in a significant underestimate of tectonic strain based on fault distribution and scarp height (e.g., Escartín et al., 2007; Medynski et al., 2016; Dumont et al., 2019).

7.2 Changing modes of lava emplacement and Layer 2A properties

The bathymetry and seafloor images (Figures 2, 3, 4 and 6) clearly show an along-axis transition from sheet- to pillow-dominated lava emplacement between the segment center and areas off to the North and South. This transition coincides with a larger-scale morphological change from smooth and regularly faulted terrain, to a rougher one dominated by hummocks and volcanic ridges. This likely reflects a gradual decrease in eruption rates (e.g., Gregg and Fink, 1995) away from the segment center, where the crust is thicker and the overall melt supply is inferred to be higher than at the segment ends. Off-axis camera tow images also suggest that these along-axis variations are persistent over time (Figure 6).

Differences in lava morphology (sheet flows vs. pillow lavas) probably result in a volcanic upper crust that differs depending on the dominant lava type, that may impact the seismic properties of Layer 2A (Figure 8a). Sheet flows efficiently fill fissures, depressions, and other small-scale topographic features. Successive sheet flows will therefore show a two-dimensional structure, with sub-horizontal interfaces (cracks), and a smooth, planar seafloor (Figure 8c left) as observed at the Lucky Strike segment (Figure 2 a and b). In contrast, an upper crust dominated by the emplacement of pillow lavas will be associated with a three-dimensional porosity structure (sub-spherical spaces between pillows) and significant topographic relief (no lateral lava transport, local emplacement; Figure 8c right). Global seismic studies do not reveal a significant difference in overall Layer 2A seismic velocity across spreading rates and sites, possibly due to numerous other local factors that also impact seismic velocity, such as alteration, faulting, fissuring, hydrothermal activity, etc. (see Christeson et al., 2019, and references therein). Furthermore, lava flows, in particular lobate ones, may show significant voids due to lava drain and collapse of the volcanic surface. Site-specific studies are thus required to correlate local variations of seismic properties with other observables.

Figure 8c presents a simplified sketch of two end-member models and a transitional one, depicting the internal structure and nature of the volcanic upper crust and of the possible impact on Layer 2A seismic properties. These models may apply to different positions along the Lucky Strike segment and may be valid for other slow- and ultra-slow spreading ridge segments with locally high melt supply. For example, crack shape and

404 orientation have a strong control on seismic velocity, as well-aligned, elongated planar
405 cracks efficiently slow-down wave propagation in directions perpendicular to them
406 relative to units with equant porosity. At the same time, seismic velocity is also controlled
407 by overall porosity. Hence, while an upper crust formed by successive sheet flows may
408 have lower porosity and hence higher seismic velocities than a 'regular' ridge section
409 with pillow lavas, the anisotropy associated with the sub-horizontal sheet flows (which
410 may be assimilated to elongated cracks) may instead lower these seismic velocities in the
411 vertical direction, perpendicular to flows (cracks). The presence of abundant sub-
412 horizontal lava flows may also increase the internal seismic reflectivity of these units. The
413 competing effect of porosity and crack shape on upper crust seismic structure may thus
414 depend on the detailed internal structure of the upper crust that is formed through
415 complex interaction of different modes of lava emplacement with faulting (Figure 8c).

416 Figure 8a shows the two-way travel time (TTWT) difference between the seafloor and the
417 Layer2A/2B boundary identified along the axis of the Lucky Strike central volcano (Seher
418 et al., 2010c). While the data shows significant scatter, there is a significant increase of
419 ~0.1 km/s of the TWTT ~15 km from the segment center (Figure 8a and b), and both
420 towards the North and South. This TWTT may be attributed to an increase in Layer 2A
421 thickness away from the ridge, to a reduction of the overall seismic velocity of this layer,
422 or to a combination of both. Seismic velocity studies indicate an anomalously thick layer
423 2A associated with the central volcano (~750-800 m), as well as anomalously low seismic
424 velocities (~2 km/s) that are attributed to the intense faulting (Arnulf et al., 2014). While

this excess Layer 2A thickness reported by Arnulf et al. (2014) is consistent with the presence of the central volcano, the TWTT increase away from the axis seems inconsistent with the focusing of melt to the segment center, where enhanced volcanism is expected, and the reduced melt supply at the segment ends where a thinner Layer 2A may develop instead. Therefore, this TTWT difference variation may be related to the change in the volcanic style instead of the Layer 2A thickness. With the increasing abundance of pillow lavas away from the segment center, that are associated with hummocky terrain and volcanic ridges, Layer 2A along the Lucky Strike segment may show lower overall seismic velocities, consistent with this TWTT difference increase (blue dashed lines in Figure 8a).

Acknowledgements: *This paper benefitted from datasets acquired during numerous cruises (Lustre'96, Graviluck'06, Bathyluck'08 and Bathyluck'09) and we thank the work of crews, officers, technical staff and science parties. We also benefitted from discussions with D. Fornari and A. Soule in the early stages of this project. This paper was improved after thorough and constructive reviews by J. Karson and B. Chadwick, in addition to the Editor's comments. Cruises were supported by NSF, USA (Lustre'96), and by the French Ministry of Research (rest of the cruises). The data analyses and research were supported by CNRS (JE, MC), U. of Bergen (TB), and both IPGP and U. Paris Diderot (CG).*

444 **References**

445 Arnulf, A.F., Harding, A.J., Kent, G.M., Singh, S.C., and Crawford, W.C., 2014.
446 Constraints on the shallow velocity structure of the Lucky Strike Volcano, Mid-
447 Atlantic Ridge, from downward continued multichannel streamer data. J. Geophys.
448 Res. Solid Earth, v. 119, no. 2, p. 1119–1144, doi: 10.1002/2013JB010500.

449 Asada, M., Yoshikawa, S., Mochizuki, N., Nogi, Y., and Okino, K., 2015, Examination of
450 Volcanic Activity: AUV and Submersible Observations of Fine-Scale Lava Flow
451 Distributions Along the Southern Mariana Trough Spreading Axis, in Ishibashi, J.,
452 Okino, K., and Sunamura, M. eds., Subseafloor Biosphere Linked to Hydrothermal
453 Systems, Springer Japan, Tokyo, p. 469–478.

454 Atwater, T., 1979, Constraints from the Famous area concerning the structure of the
455 oceanic section, in p. 33–42.

456 Ballard, R.D., Bryan, W.B., Heirtzler, J.R., Keller, G., Moore, J.G., van Andel, T., 1975.
457 Manned submersible observations in the FAMOUS Area: Mid-Atlantic Ridge.
458 Science, v. 190, 103–108.

459 Ballard, R.D., Holcomb, R.T., van Andel, T.H., 1979. The Galapagos rift at 86°W 2. Sheet
460 flows, collapse pits, and lava lakes of the rift valley. J. Geophys. Res. 84, 5407–5422.

461 Barberi, F., and Varet, J., 1971. The Erta Ale volcanic range (Danakil Depression, Northern
462 Afar, Ethiopia). Bulletin Volcanologique, v. 34, no. 4, p. 848–917.

463 Barreyre, T., Escartín, J., Garcia, R., Cannat, M., Mittelstaedt, E., and Prados, R.,
464 2012. Structure, temporal evolution, and heat flux estimates from the Lucky Strike
465 deep-sea hydrothermal field derived from seafloor image mosaics. Geochem.
466 Geophys. Geosyst., 13, Q04007, doi:10.1029/2011GC003990.

467 Bideau, D., Hékinian, R., Sichler, B., Gràcia, E., Bollinger, C., Constantin, M., and Guivel,
468 C., 1998, Contrasting volcanic-tectonic processes during the past 2 Ma on the Mid-
469 Atlantic Ridge: submersible mapping, petrological and magnetic results at lat.
470 34°52′N and 33°55′N: Marine Geophysical Researches, v. 20, p. 425–458.

471 Bonatti, E., Harrison, C.G.A., 1988. Eruption styles of basalt in oceanic spreading ridges
472 and seamounts: Effect of magma temperature and viscosity. J. Geophys. Res. 93,
473 2967. https://doi.org/10.1029/JB093iB04p02967

474 Cannat, M., Briais, A., Deplus, C., Escartín, J., Georgen, J., Lin, J., Mercouriev, S., Meyzen,
475 C., Muller, M., Pouliquen, G., Rabain, A., and Da Silva, P., 1999. Mid-Atlantic Ridge-
476 Azores hotspot interactions: Along-axis migration of a hotspot-derived event of
477 enhanced magmatism 10 to 4 Ma ago. Earth and Planetary Science Letters, v. 173, no.
478 3, doi: 10.1016/S0012-821X(99)00234-4.

479 Cannat, M., Sauter, D., Bezos, A., Meyzen, C., Humler, E., and Le Rigoleur, M.,
480 2008. Spreading rate, spreading obliquity, and melt supply at the ultraslow
481 spreading Southwest Indian Ridge. Geochem. Geophys. Geosyst., 9, Q04002,
482 doi:10.1029/2007GC001676.

Chadwick William W., J., 2003, Quantitative constraints on the growth of submarine lava pillars from a monitoring instrument that was caught in a lava flow: Journal of Geophysical Research, v. 108, no. B11, p. 2534, doi:10.1029/2003JB002422.

Chadwick, W.W., Gregg, T.K.P., Embley, R.W., 1999. Submarine lineated sheet flows: a unique lava morphology formed on subsiding lava ponds. Bull. of Volcanol. 61, 194–206. https://doi.org/10.1007/s004450050271

Chen, J., Cannat, M., Tao, C., Sauter, D., and Munschy, M., 2021. 780 thousand years of upper-crustal construction at a melt-rich segment of the ultraslow spreading Southwest Indian Ridge 50°28'E, J. Geophys. Res. Solid Earth, doi: 10.1029/2021JB022152.

Christeson, G.L., Goff, J.A., and Reece, R.S., 2019, Synthesis of Oceanic Crustal Structure From Two-Dimensional Seismic Profiles: Reviews of Geophysics, v. 57, no. 2, p. 504–529, doi: 10.1029/2019RG000641.

Clague, D., Paduan, J., Caress, D., Chadwick, W., Le Saout, M., Dreyer, B., Portner, R., 2017. High-Resolution AUV Mapping and Targeted ROV Observations of Three Historical Lava Flows at Axial Seamount. Oceanography 30. https://doi.org/10.5670/oceanog.2017.426

Combier, V., Seher, T., Singh, S.C., Crawford, W.C., Cannat, M., Escartín, J., and Dusunur, D., 2015. Three-dimensional geometry of axial magma chamber roof and faults at

Lucky Strike volcano on the Mid-Atlantic Ridge. J. Geophys. Res. Solid Earth, v. 120, no. 8, doi: 10.1002/2015JB012365.

Crane, K., and Ballard, R.D., 1981, Volcanics and structure of the FAMOUS narrowgate rift: evidence for cyclic evolution: AMAR 1: Journal of Geophysical Research, v. 86, no. B6, p. 5112–5124.

Crane, K., Johnson, L., Appelgate, B., Nishimura, C., Buck, R., Jones, C., Vogt, P., and Kos'yan, R., 1997, Volcanic and Seismic Swarm Events on the Reykjanes Ridge and Their Similarities to Events on Iceland: Results of a Rapid Response Mission: Marine Geophysical Research, v. 19, no. 4, p. 319–338, doi: 10.1023/A:1004298425881.

Crawford, W.C., Singh, S.C., Seher, T., Combier, V., Dusunur, D., Cannat, M., Rona, P., Devey, C.W., Dyment, J., and Murton, B., 2010. Crustal structure, magma chamber and faulting beneath the Lucky Strike hydrothermal fields, in Diversity of Hydrothermal Systems on Slow Spreading Ocean Ridges, AGU, Washington DC, p. 113–132.

Davey, S., Ernst, R. et Samson, C., 2011. « Radiating graben-fissure system in Imdr Regio, Venus ». Communication lors de la conférence : Advances in Earth Sciences Research Conference (Ottawa, ON, Canada, Mar. 25-27, 2011).

519 Detrick, R.S., Needham, H.D., Renard, V., 1995. Gravity anomalies and crustal thickness
520 variations along the Mid-Atlantic ridge between 33°N and 40°N. J. Geophys. Res.
521 100, 3767–3787.

522 Deschamps, A., Tivey, M., Embley, R.W., Chadwick, W.W., 2007. Quantitative study of
523 the deformation at Southern Explorer Ridge using high-resolution bathymetric data.
524 Earth and Planetary Science Letters, 259, 1–17.
525 https://doi.org/10.1016/j.epsl.2007.04.007

526 Dumont, S., Klinger, Y., Socquet, A., Escartín, J., Grandin, R., Jacques, E., Medynski, S.,
527 and Doubre, C., 2019. Rifting Processes at a Continent-Ocean Transition Rift
528 Revealed by Fault Analysis: Example of Dabbahu-Manda-Hararo Rift (Ethiopia).
529 Tectonics, v. 38, no. 1, p. 190–214, doi: 10.1029/2018TC005141.

530 Edwards, M.H., Kurras, G.J., Tolstoy, M., Bohnenstiehl, D., Coakley, B.J., and Cochran,
531 J.R., 2001. Evidence of recent volcanic activity on the ultra-slow Gakkel ridge:
532 Nature, v. 409, p. 808–812. https://doi.org/10.1038/35057258.

533 Embley, R.W., Murphy, K.M., and Fox, C.G., 1990, High-resolution studies of the summit
534 of Axial Volcano: Journal of Geophysical Research, v. 95, no. B8, p. 12785, doi:
535 10.1029/JB095iB08p12785.

536 Escartín, J., Soule, S.A., Fornari, D.J., Tivey, M.A., Schouten, H., and Perfit, M.R., 2007.
537 Interplay between faults and lava flows in construction of the upper oceanic crust:

538 The East Pacific Rise crest 9°25′-9°58′N. Geochem. Geophys. Geosyst., v. 8, no. 6, doi:
539 10.1029/2006GC001399.

540 Escartín, J., Soule, S.A., Cannat, M., Fornari, D.J., Düşünür, D., and Garcia, R., 2014. Lucky
541 Strike seamount: Implications for the emplacement and rifting of segment-centered
542 volcanoes at slow spreading mid-ocean ridges. Geochem. Geophys. Geosyst., v. 15,
543 no. 11, p. 4157–4179, doi: 10.1002/2014GC005477

544 Escartín, J., Barreyre, T., Cannat, M., Garcia, R., Gracias, N., Deschamps, A., Salocchi, A.,
545 Sarradin, P.-M., Ballu, V., 2015. Hydrothermal activity along the slow-spreading
546 Lucky Strike ridge segment (Mid-Atlantic Ridge): Distribution, heatflux, and
547 geological controls. Earth and Planetary Science Letters, 431, 173–185.
548 https://doi.org/10.1016/j.epsl.2015.09.025

549 Estep, J., Reece, R., Kardell, D.A., Christeson, G.L., and Carlson, R.L., 2019. Seismic Layer
550 2A: Evolution and Thickness From 0- to 70-Ma Crust in the Slow-Intermediate
551 Spreading South Atlantic. J. Geophys. Res. Solid Earth, v. 124, no. 8, p. 7633–7651,
552 doi: 10.1029/2019JB017302

553 Fornari, D.J., 1986. Submarine lava tubes and channels. Bull. of Volcanol., v. 48, p. 291–
554 298.

555 Gràcia, E., Parson, L.M., Bideau, D., and Hekinian, R., 1998, Volcano-tectonic variability
556 along segments of the Mid-Atlantic Ridge between Azores platform and Hayes

fracture zone: evidence from submersible and high-resolution sidescan sonar data (R. A. Mills & K. Harrison, Eds.): Geological Society, London, Special Publications, v. 148, no. 1, p. 1–15, doi: 10.1144/GSL.SP.1998.148.01.01.

Gregg, T.K.P., Fink, J.H., 1995. Quantification of submarine lava-flow morphology through analog experiments. Geology 23, 73. https://doi.org/10.1130/0091-7613(1995)023<0073:QOSLFM>2.3.CO;2

Gregg, T.K.P., Fink, J.H., Griffiths, R.W., 1998. Formation of multiple fold generations on lava flow surfaces: Influence of strain rate, cooling rate, and lava composition. J. Volcanol. Geotherm. Res. 80, 281–292.

Gregg, T.K.P., Fornari, D.J., 1998. Long submarine lava flows: Observations and results from numerical modeling. J. Geophys. Res. Solid Earth 103, 27517–27531. https://doi.org/https://doi.org/10.1029/98JB02465

Grevemeyer, I., Kaul, N., Villinger, H., Weigel, W., 1999. Hydrothermal activity and the evolution of the seismic properties of upper oceanic crust. J. Geophys. Res. 104, 5069–5079, doi:10.1029/1998JB900096

Griffiths, R.W., Fink, J.H., 1992. Solidification and morphology of submarine lavas: A dependence on extrusion rate. J. Geophys. Res. 97, 19729. https://doi.org/10.1029/92JB01594

575 Hooft, E.E.E., Schouten, H., and Detrick, R.S., 1996. Constraining crustal emplacement
576 processes from the variation in Layer 2A thickness at the East Pacific Rise. Earth and
577 Planetary Science Letters, v. 142, p. 289–309, https://doi.org/10.1016/0012-
578 821x(96)00101-x

579 Humphris, S.E., Fornari, D.J., Scheirer, D.S., German, C.R., and Parson, L.M., 2002.
580 Geotectonic setting of hydrothermal activity on the summit of Lucky Strike
581 seamount (37°17′N, Mid-Atlantic Ridge). Geochem. Geophys. Geosyst., v. 3, no. 8,
582 doi: 10.1029/2001GC000284.

583 Hussenoeder, S.A., Kent, G.M., and Detrick, R.S., 2002. Upper crustal seismic structure of
584 the slow-spreading Mid-Atlantic Ridge, 35°N: Constraints on volcanic emplacement
585 processes. J. Geophys. Res., v. 107, no. B8, doi: 10.1029/2001JB001691

586 Kent, G.M., Harding, A.J., Orcutt, J.A., Detrick, R.S., Mutter, J.C., and Buhl, P., 1994.
587 Uniform accretion of oceanic crust south of the Garrett transform at 14°15′S on the
588 East Pacific Rise. J. Geophys. Res., v. 99, no. B5, p. 9097–9116.

589 Kurras, G.J., RFornari, D.J., Edwards, M.H., Perfit, M.R., and Smith, M.C., 2000, Volcanic
590 morphology of the East Pacific Rise Crest 9°49′-52′: Implications for volcanic
591 emplacement processes at fast-spreading mid-ocean ridges: Marine Geophysical
592 Researches, v. 21, p. 23–41.

593 Langmuir, C., Humphris, S., Fornari, D., Van Dover, C., Von Damm, K., Tivey, M.K.,
594 Colodner, D., Charlou, J. -l., Desonie, D., Wilson, C., Fouquet, Y., Klinkhammer, G.,
595 and Bougault, H., 1997. Hydrothermal vents near a mantle hot spot: the Lucky Strike
596 vent field at 37°N on the Mid-Atlantic Ridge. Earth and Planetary Science Letters, v.
597 148, p. 69–91, https://doi.org/10.1016/S0012-821X(97)00027-7

598 Lonsdale, P., 1977. Abyssal pahoehoe with lava coils at the Galapagos rift. Geology 5,
599 147–152.

600 Medynski, S., Pik, R., Burnard, P., Dumont, S., Grandin, R., Williams, A., Blard, P.-H.,
601 Schimmelpfennig, I., Vye-Brown, C., France, L., Ayalew, D., Benedetti, L., and Yirgu,
602 G., 2016. Magmatic cycles pace tectonic and morphological expression of rifting
603 (Afar depression, Ethiopia). Earth and Planetary Science Letters, v. 446, p. 77–88, doi:
604 10.1016/j.epsl.2016.04.014

605 Mège, D., Cook, A. C., Garel, E., Lagabrielle, Y., and Cormier, M.-H., 2003. Volcanic
606 rifting at Martian grabens. J. Geophys. Res., 108, 5044, doi:10.1029/2002JE001852, E5.

607 Okubo, C.H., Martel, S.J., 1998. Pit crater formation on Kilauea volcano, Hawaii. J.
608 Volcanol. Geotherm. Res. 86, 1–18.

609 Ondréas, H., Cannat, M., Fouquet, Y., Normand, A., Sarradin, P.-M., Sarrazin, J., 2009.
610 Recent volcanic events and the distribution of hydrothermal venting at the Lucky

611 Strike hydrothermal field, Mid-Atlantic Ridge. Geochem. Geophys. Geosyst. 10,
612 Q02006, doi:10.1029/2008GC002171.

613 Peirce, C., Sinha, M., Topping, S., and Gill, C., 2007. Morphology and genesis of slow-
614 spreading ridges—seabed scattering and seismic imaging within the oceanic crust.
615 Geophysical Journal International, v. 168, p. 59–89, doi: 10.1111/j.1365-
616 246X.2006.03223.x

617 Sauter, D., Cannat, M., Rouméjon, S. et al., 2013. Continuous exhumation of mantle-
618 derived rocks at the Southwest Indian Ridge for 11 million years. Nature
619 Geosci. 6, 314–320. https://doi.org/10.1038/ngeo1771

620 Searle, R.C., Murton, B.J., Achenbach, K., LeBas, T., Tivey, M., Yeo, I., Cormier, M.H.,
621 Carlut, J., Ferreira, P., Mallows, C., Morris, K., Scroth, N., van Calsteren, P., and
622 Walters, C., 2010. Structure and development of an axial volcanic ridge: Mid-Atlantic
623 Ridge, 45°N. Earth and Planetary Science Letters, v. 209, p. 228–241,
624 https://doi.org/10.1016/j.epsl.2010.09.003

625 Seher, T., Crawford, W.C., Singh, S.C., Cannat, M., Combier, V., and Dusunur, D., 2010a.
626 Crustal velocity structure of the Lucky Strike segment of the Mid-Atlantic Ridge at
627 37 N from seismic refraction measurements. J. Geophys. Res., v. 115, p. B03103,
628 doi:10.1029/2009JB006650.

629 Seher, T., Singh, S.C., Crawford, W.C., and Escartín, J., 2010b. Upper crustal velocity
630 structure beneath the central Lucky Strike Segment from seismic refraction
631 measurements. Geochem. Geophys. Geosyst., v. 11, no. 5, p. Q05001, doi:
632 10.1029/2009GC002894.

633 Seher, T., Crawford, W.C., Singh, S.C., and Cannat, M., 2010c. Seismic layer 2A variations
634 in the Lucky Strike segment at the Mid-Atlantic Ridge from reflection measurements.
635 J. Geophys. Res., v. 115, p. B07107, doi: 10.1029/2009JB006783

636 Singh, S., Crawford, W., Carton, H., Seher, T., Combier, V., Cannat, M., Canales, J. P.,
637 Dusunur, D., Escartin, J., Miranda, J.M., 2006. Discovery of a magma chamber and
638 faults beneath a Mid-Atlantic Ridge hydrothermal field. Nature, 442, 1029–1032.
639 https://doi.org/10.1038/nature05105

640 Smith, D.K., and Cann, J.R., 1992. The role of seamount volcanism in crustal construction
641 at the Mid-Atlantic Riddge (24°N-30°N). J. Geophys. Res., v. 97, p. 1645–1658.

642 Smith, D.K., and Cann, J.R., 1993, Building the crust at the Mid-Atlantic Ridge: Nature
643 365, p. 707–715.

644 Soule, S.A., Fornari, D.J., Perfit, M.R., Tivey, M.A., Ridley, W.I., Schouten, H., 2005.
645 Channelized lava flows at the East Pacific Rise crest 9°-10°N: The importance of off-
646 axis lava transport in developing the architecture of young oceanic crust. Geochem.
647 Geophys. Geosyst., 6, https://doi.org/10.1029/2005GC000912

Soule, S.A., Fornari, D.J., Perfit, M.R., Rubin, K.H., 2007. New insights into mid-ocean ridge volcanic processes from the 2005–2006 eruption of the East Pacific Rise, 9°46′N–9°56′N. Geology 35, 1079. https://doi.org/10.1130/G23924A.1

Soule, S.A., Escartín, J., and Fornari, D.J., 2009. A record of eruption and intrusion at a fast-spreading ridge axis: the axial summit trough of the East Pacific Rise 9˚-10˚N. Geochem. Geophys. Geosyst., v. 10, no. 10, p. Q10T07, doi:10.1029/2008GC002354.

Stakes, D.S., Shervais, J.W., and Hopson, C.A., 1984, The volcanic-tectonic cycle of the FAMOUS and AMAR valleys, Mid-Atlantic Ridge (36°47′N): Evidence from basalt glass and phenocryst compositional variations for a steady state magma chamber beneath the valley midsections, AMAR3: Journal of Geophysical Research, v. 89, no. B8, p. 6995–7028.

Wilkens, R. H., Fryer, G. J., and Karsten, J., 1991. Evolution of porosity and seismic structure of upper oceanic crust: Importance of aspect ratios. J. Geophys. Res., 96(B11), 17981– 17995, doi:10.1029/91JB01454

White, S.M., Haymon, R.M., Fornari, D.J., Perfit, M.R., and Macdonald, K.C., 2002, Correlation between volcanic and tectonic segmentation of fast-spreading ridges: evidence from volcanic structures and lava flow morphology on the East Pacific Rise at 9°-10°N: Journal of Geophysical Research, v. 107, no. B8, p. 10.1029/2001JB000571.

Yeo, I., Searle, R.C., Achenbach, K.L., Le Bas, T.P., Murton, B.J., 2012. Eruptive hummocks: Building blocks of the upper ocean crust. Geology 40, 91–94. https://doi.org/10.1130/G31892.1

Captions and figures

***Figure 1**. a) Shipboard bathymetry of the Lucky Strike ridge segment, showing camera tow tracks (numbered red lines), Nautile submersible tracks (black lines) and VICTOR remotely operated vehicle tracks (blue lines). Numbered black circles indicate the location of images in Figure 4. b) Near-bottom multibeam bathymetry surveys (~1 m resolution) underlain by ship multibeam bathymetry (with transparency). The blue line shows the extent of the Lustre'96 DSL120 deep-towed sonar survey (Humphris et al., 2002; Escartín et al., 2014). Black boxes represent the location of Figure 2. See text and Supplementary Materials for details on cruises and datasets.*

***Figure 2.** Shaded bathymetry (left) and slope (right) maps of the central section of the Lucky Strike segment (a and b), and of the rift valley floor towards the end of the segment (c and d). See Figure 1 for locations. At the segment center (a and b), faults dissect two volcanic cones (V1 and V2) and crosscut a flat seafloor that is formed primarily by the accumulation of sheet flows (sf and pink shade in panel b; see text). This flat seafloor transitions to hummocks (h in panel b) and axial volcanic ridges towards the south, which are also faulted and fissured. This transition is indicated by the arrow labelled* t. *At the segment end (c and d) the seafloor is fully covered by hummocks, variably fissured and faulted. Hydrothermal deposits (h, orange transparency) are present at the center of the volcanic cones, and vents are indicated by red dots. Collapse pits are indicated by c. White and red boxes show the locations of Figure 3a, b and c, and the blue outlines in a) indicate the extent of seafloor optical photomosaics (pm).*

***Figure 3.** a) Shaded high-resolution bathymetry (~1m resolution) of the Lucky Strike axis along the southern flank of the central volcano (location of panels a, b and c is shown in Figure 2b)*

showing the most recent axial lava flow (a and b), and older (more sedimented) lava flows (c), and associated volcanic structures. b) Detail of the terminal portion of the axial lava flow. c) Lava flows, showing folded textures, emplaced at the base of hummock mounds. Labels correspond to location of images in Figure 4 and profiles (p) in Figure 5. Blue lines indicate location of topographic profiles in Figure 5.

Figure 4. *Examples of lava textures, tectonic and volcanic structures from seafloor imagery along the Lucky Strike segment. a) Photomosaic (ROV imagery) of the axial lava flow head, showing the main channel with lineations (yellow lines) and whorls (yellow dots at their centers), the broken-up lavas (jumbled or hackly lavas) at the flow edge (dashed white line), and the bounding fault scarp. b) Oblique view of axial lava flow (Nautile video grab, dive#1624). c) Partially sedimented and faulted off-axis sheet flow with lava coils, adjacent to a fault scarp to the right (OTUS photomosaic). d) Lobate flows (CT#7). e) Pillow lavas on the flanks of a volcanic ridge, elongated in the downhill flow direction (CT#4). f) Collapse pit along a dike-related graben system (OTUS photomosaic, Bathyluck'09). Locations of images are shown in Figs. 1 (d, e) and 3 (a,-c, f).*

Figure 5. *a) Profile along the center of the youngest axial flow, showing the location of the across-flow profiles in b) and two of the detailed along-flow profiles in c). b) Across-flow profiles show the change in morphology, from a wide flow with a collapsed central channel (p1) to an inflated flow, bound by fault scarps (p5-p6). c) Detailed along-flow profiles showing the amplitude (1-2 m) and wavelength (~10-20 m) of the folds in the surface of the lava flow (see Figure 3). The location of profile pc is shown in Figure 3c.*

Figure 6. *a) Along-axis bathymetry profile (top) and relative abundance of lava flow types along camera tow tracks CT01 through CT10 (locations shown in Figure 1a). b) Orientation of lineations identified both at camera tow tracks (CT#) and the photomosaics (PM) at the center of the Lucky Strike segment, and fault orientations digitized from side-scan sonar data (Escartín et al., 2014). For reference, the plot also shows the mean orientations of sheet flow lineations, faults, and the Lucky Strike segment (LS), indicated by inverted triangles, and the standard deviation when available (horizontal lines).*

Figure 7. *Recent lava flows, shaded in red, steered by fault scarps from the Afar region, a) along the rift extending SE of Hayli Gub volcano, and terminating and spreading at the sedimented Afrera Lake plain and b) along the Northern Manda-Hararo Rift, SE of Dabahu volcano. Satellite imagery: ©CNES/Airbus provided by Google Maps (accessed March 2021).*

Figure 8. *Geological interpretation of the upper oceanic crust, Layer 2A, at the Lucky Strike segment. a) Along-axis variations in Layer 2A two-way travel time (TWTT) difference between the seafloor and the Layer 2A/2B reflector (modified from Seher et al., 2010c). Towed camera transect numbers are indicated as TowCam track number). The red dashed line corresponds to the average TWTT difference for the segment center (sheet flow dominated), and the blue dashed lines highlight the gradients towards the N and S with increasing TWTT difference. b) Shaded bathymetric map from Seher et al. (2010c). c) Sketches showing the structure and construction of the upper oceanic crust at a slow-spreading ridge with high melt supply, from segment center to segment ends. Left: Sheet flow dominated seafloor, with interpreted high seismic velocity and low porosity. Middle: transitional crust between the end-members, characterized by a mix of sheet*

flows deviated from the axis and ponding around axial volcanic ridges, and pillows accreting as axial volcanic ridges. Right: Axial volcanic ridge dominated seafloor, with feeding dikes. High porosity between pillows and may be associated lower seismic velocity. Colored arrows for each model are located along the axis (a and b).

Figure 1

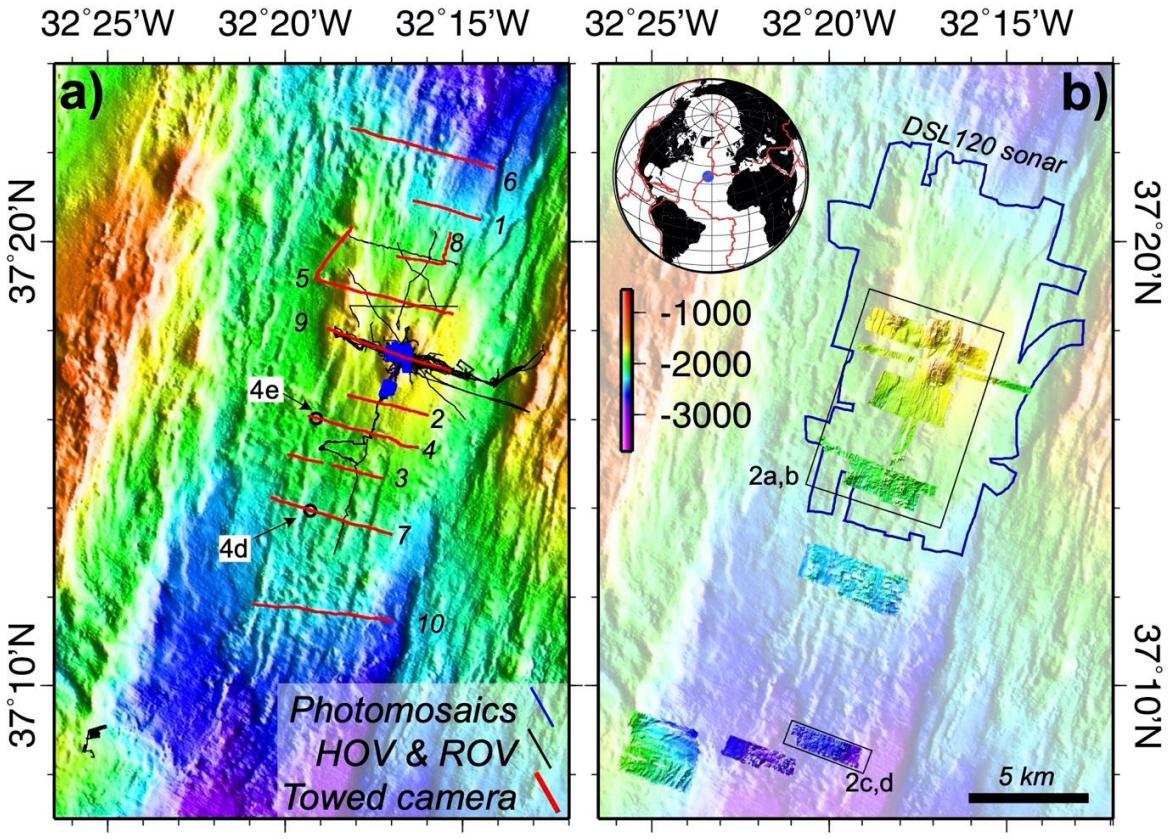

740 *Figure 2*

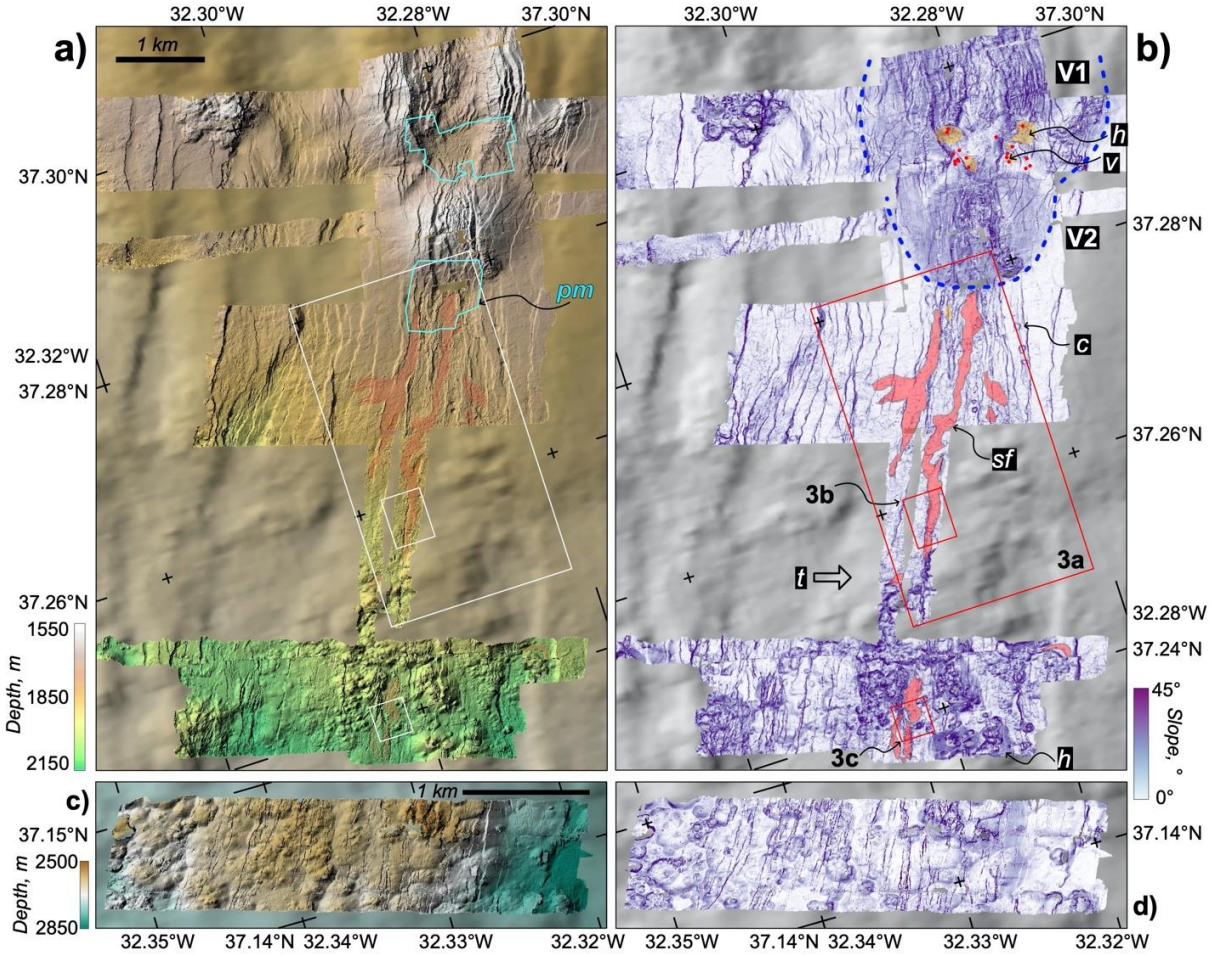

741

742 *Figure 3*

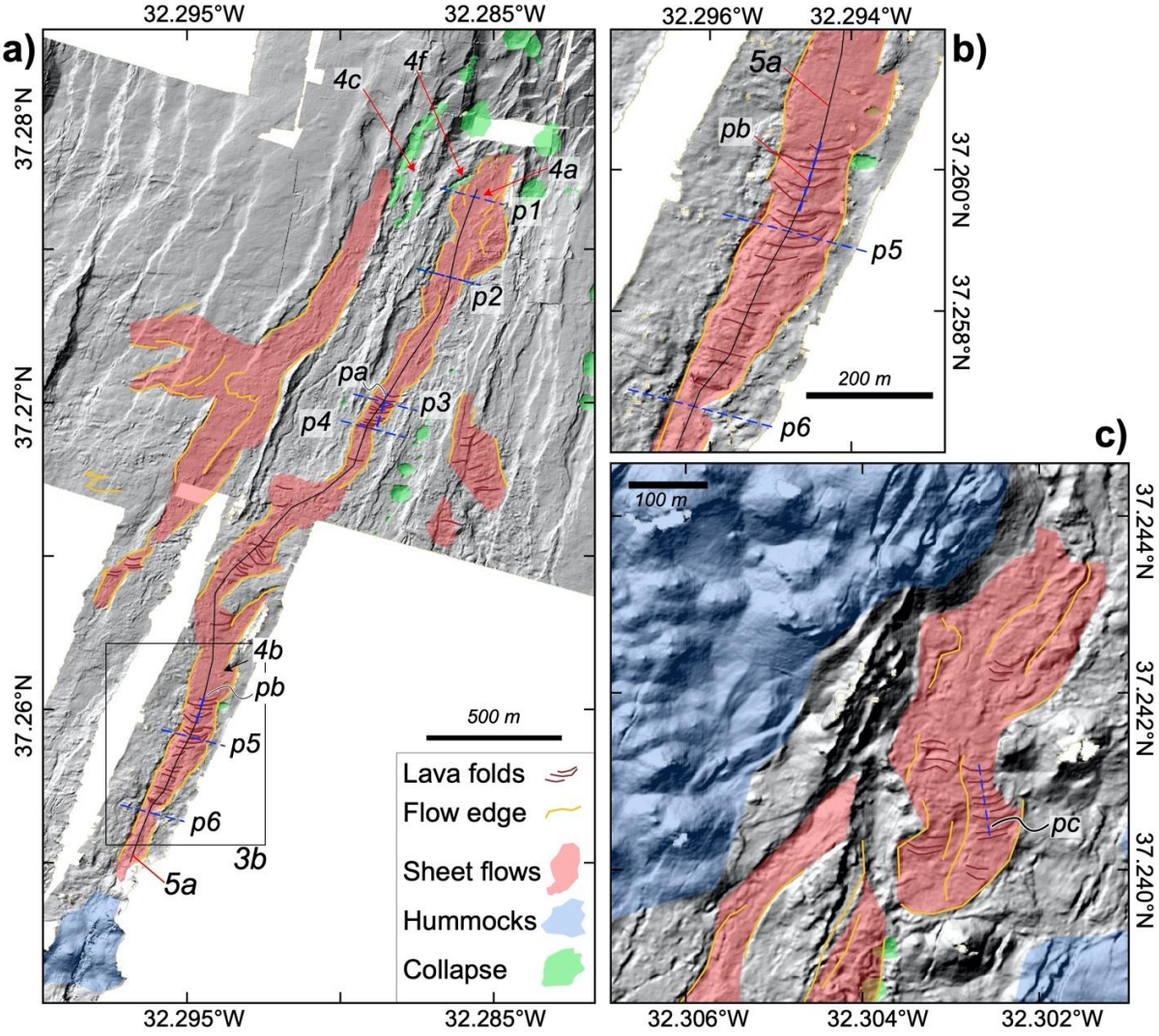

743

744 *Figure 4*

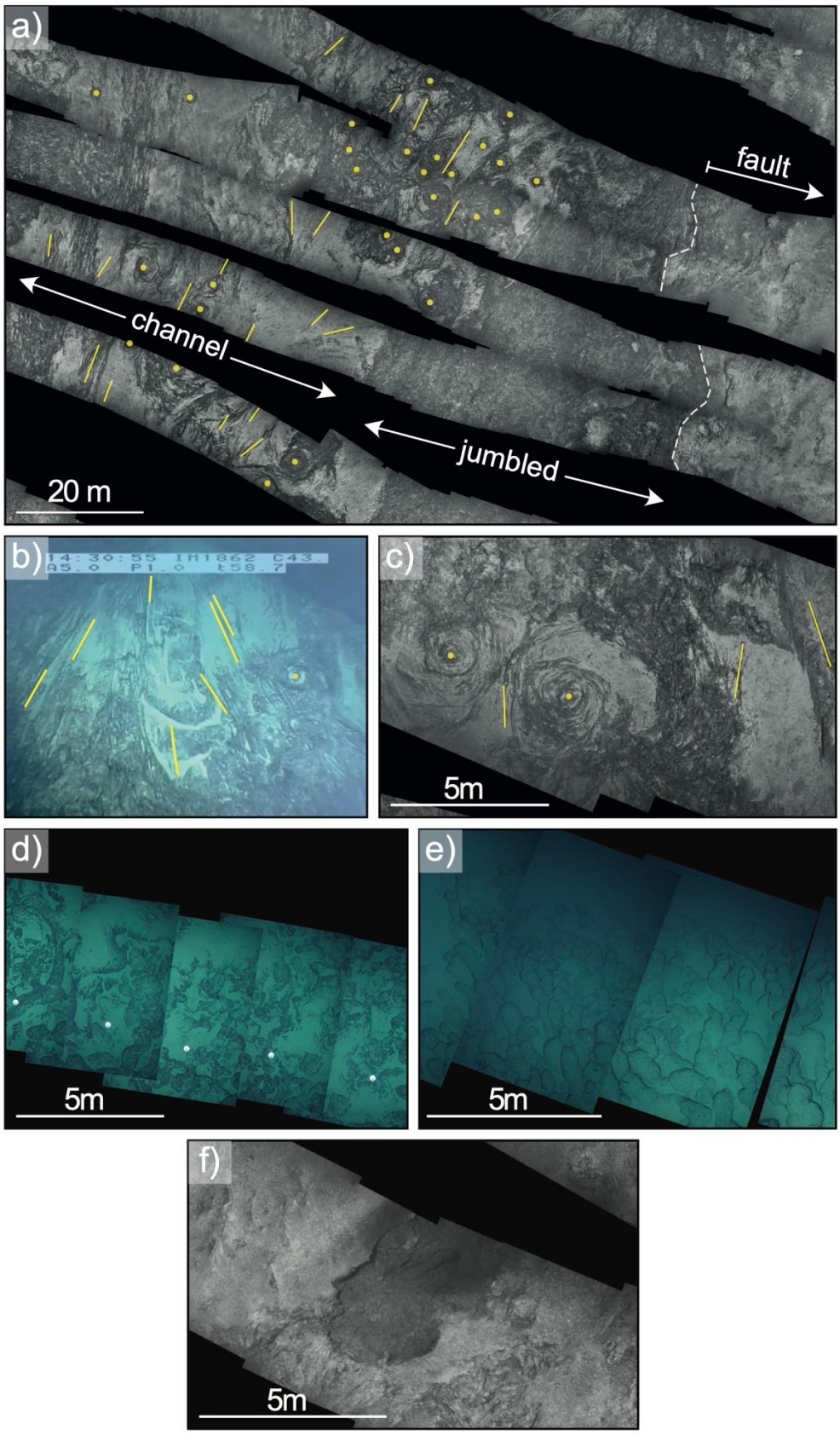

745 *Figure 5*

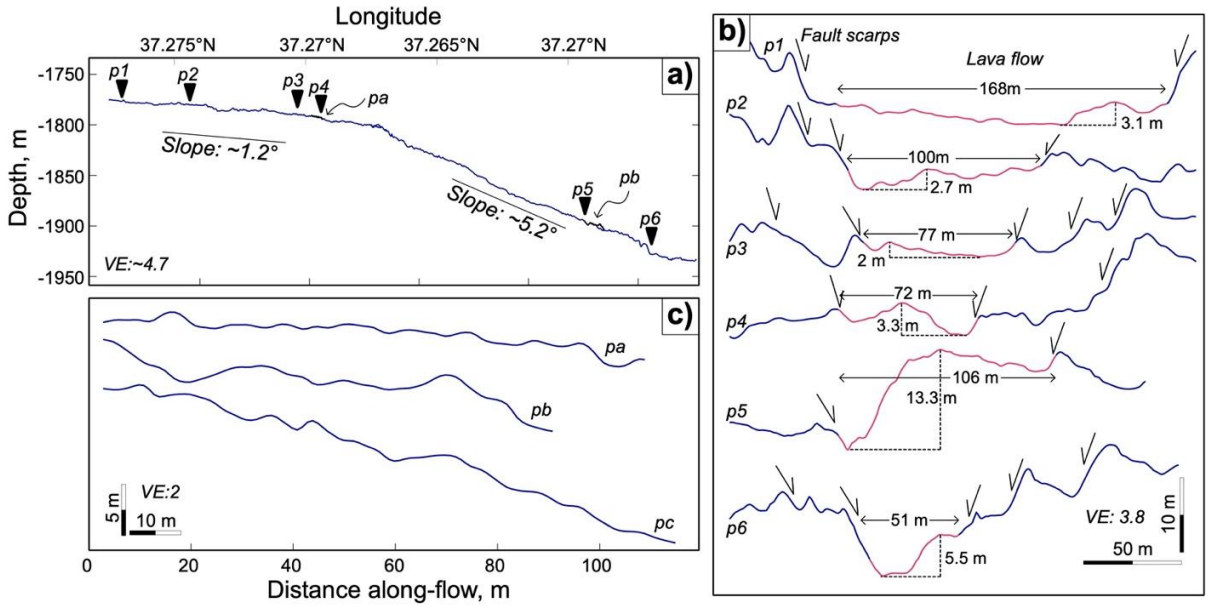

746

747 *Figure 6*

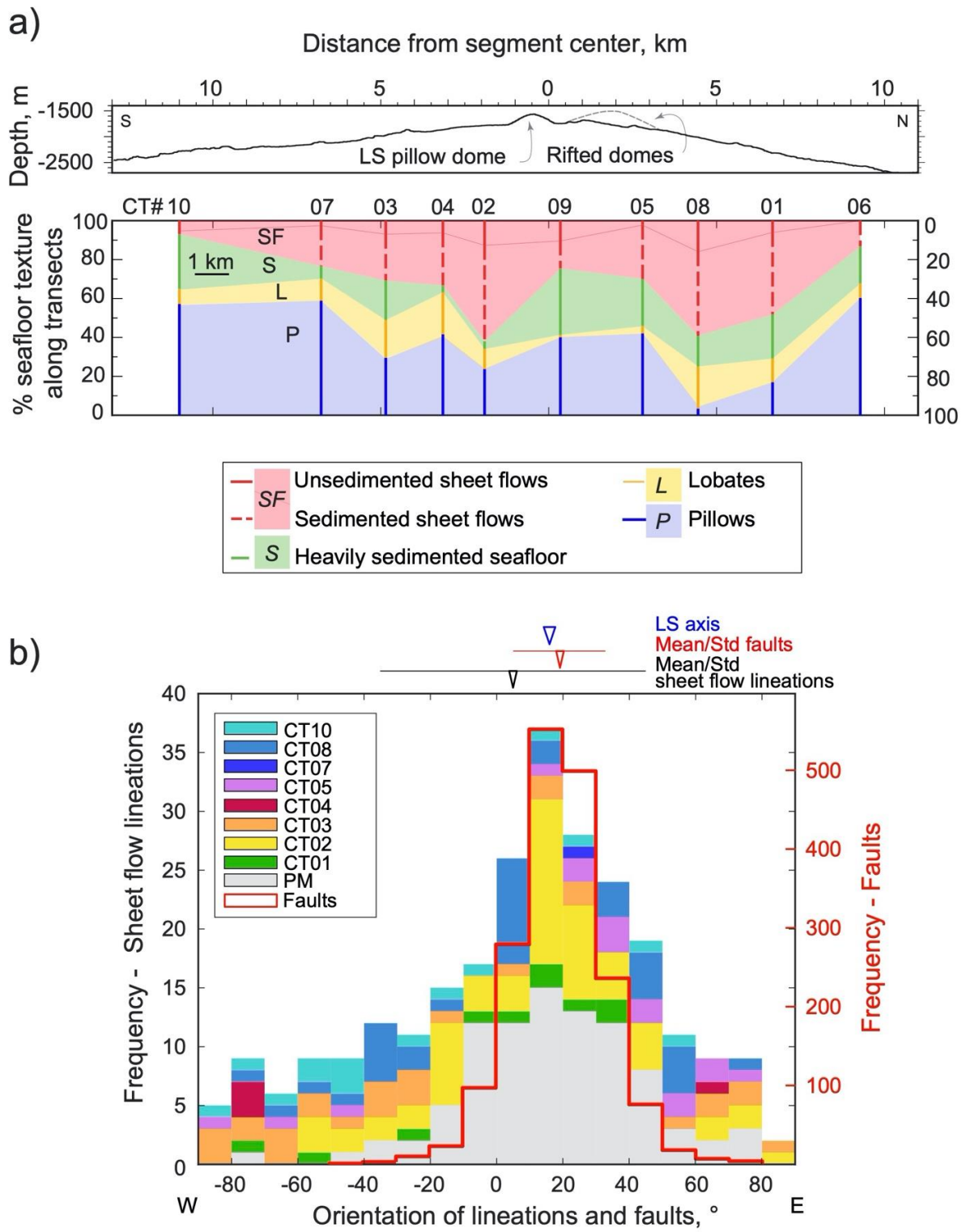

748

749 *Figure 7*

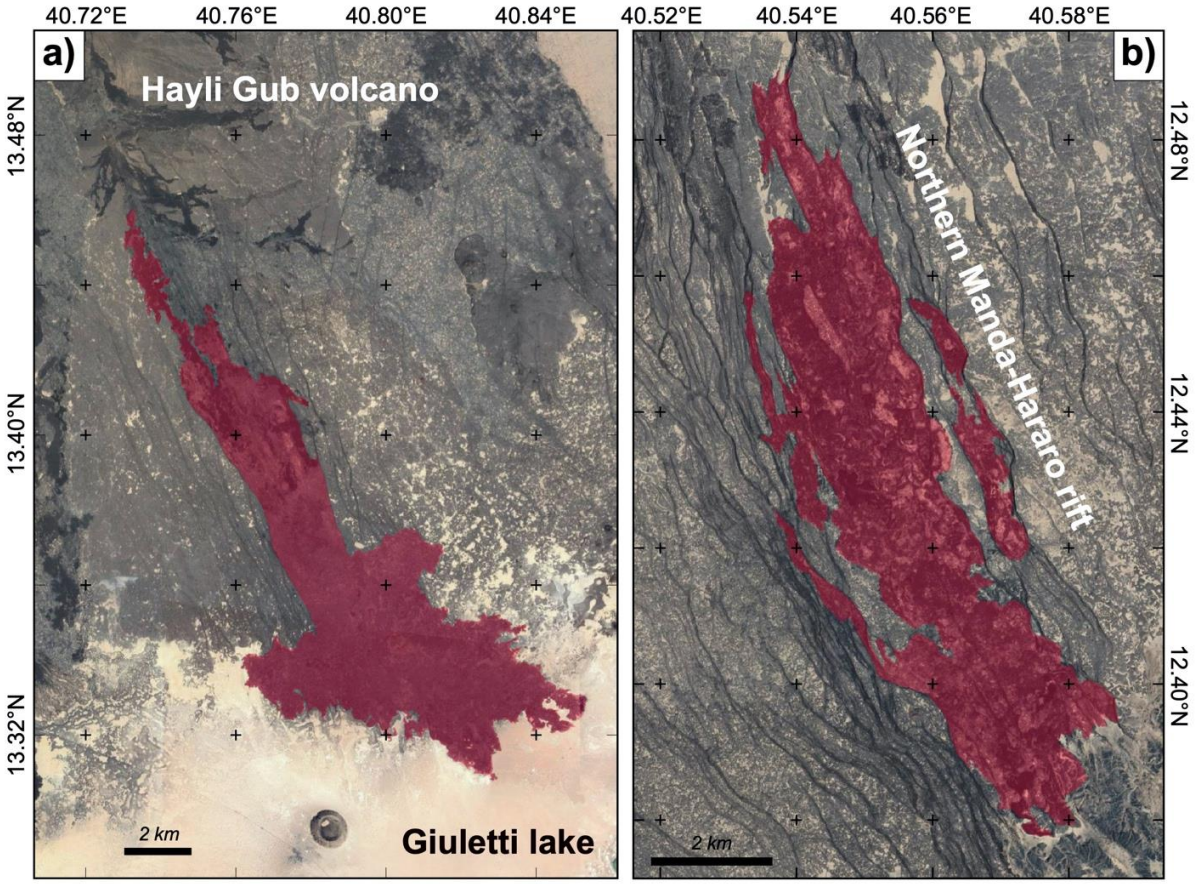

750

751 *Figure 8*

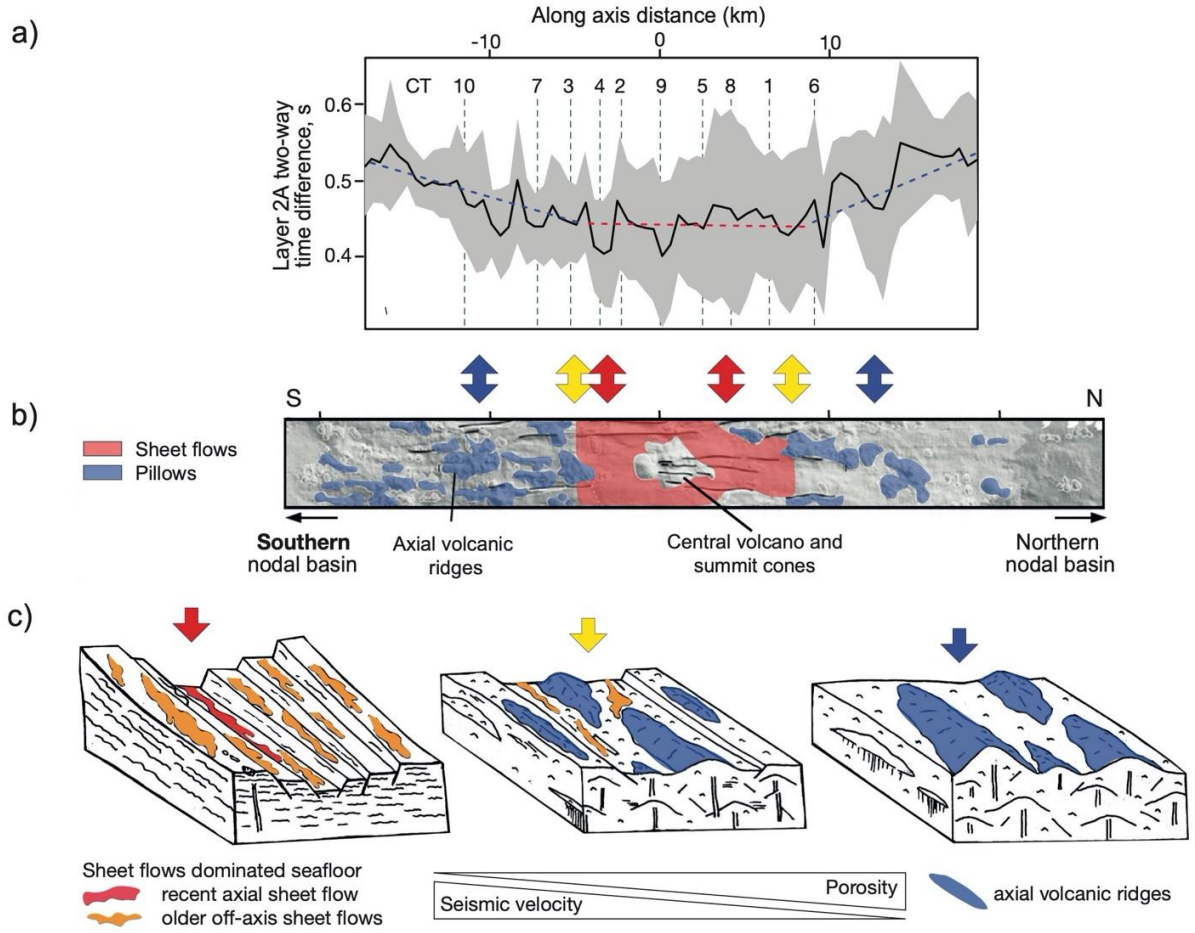

752

Figure1

Click here to access/download;Figure;Fig1.jpg

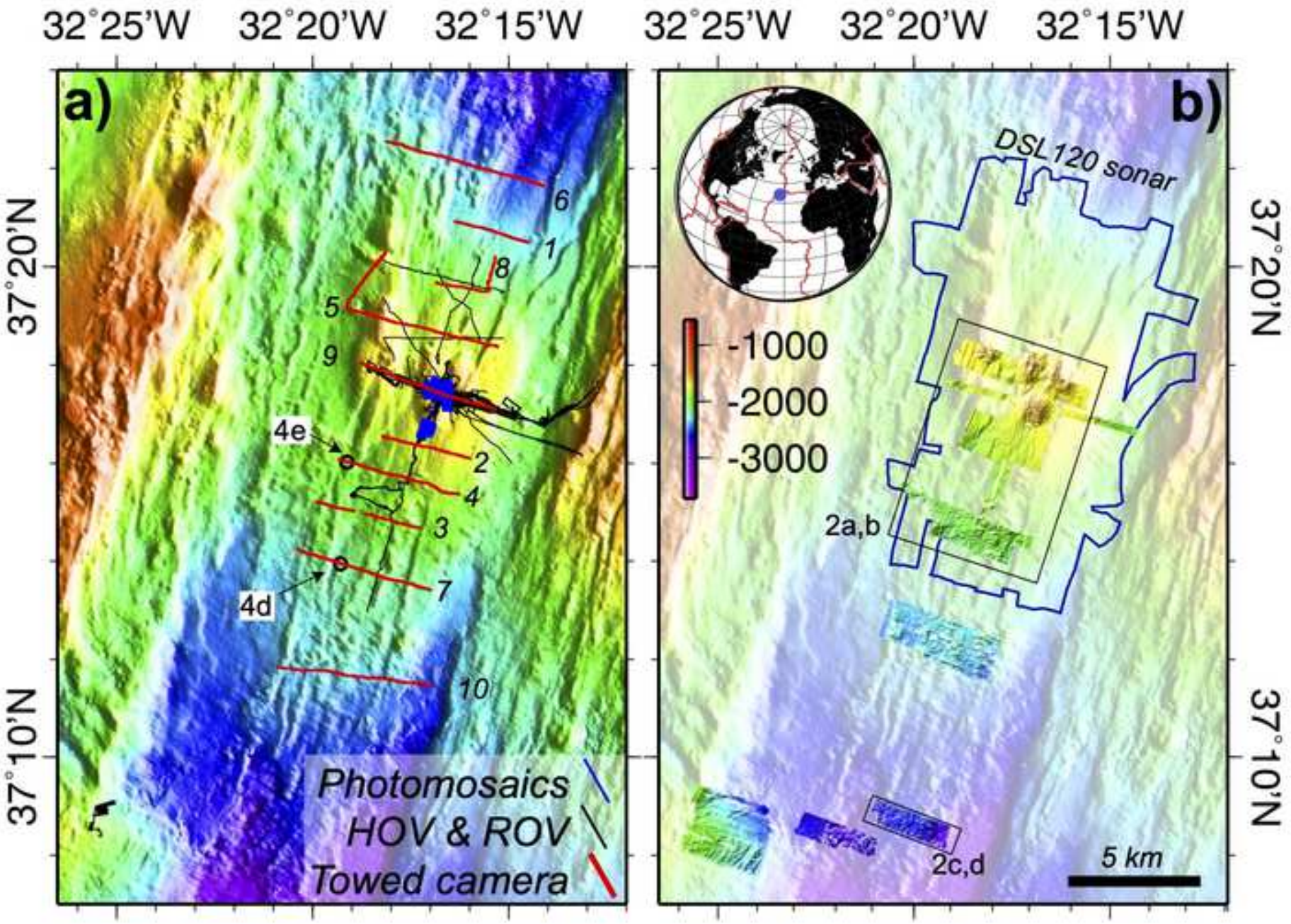

Figure2

Click here to access/download;Figure;Fig2.jpg

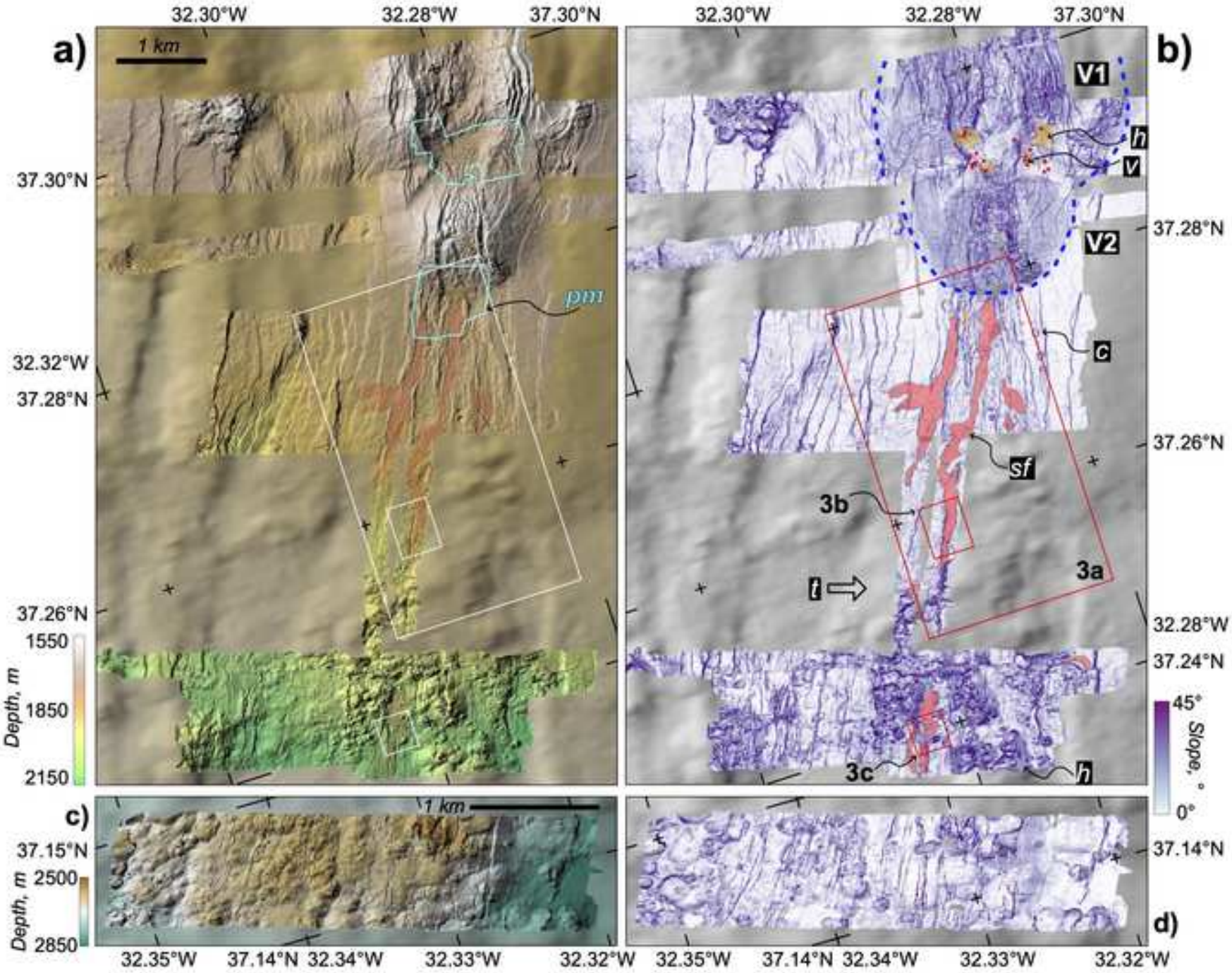

Figure3

Click here to access/download;Figure;Fig3.jpg

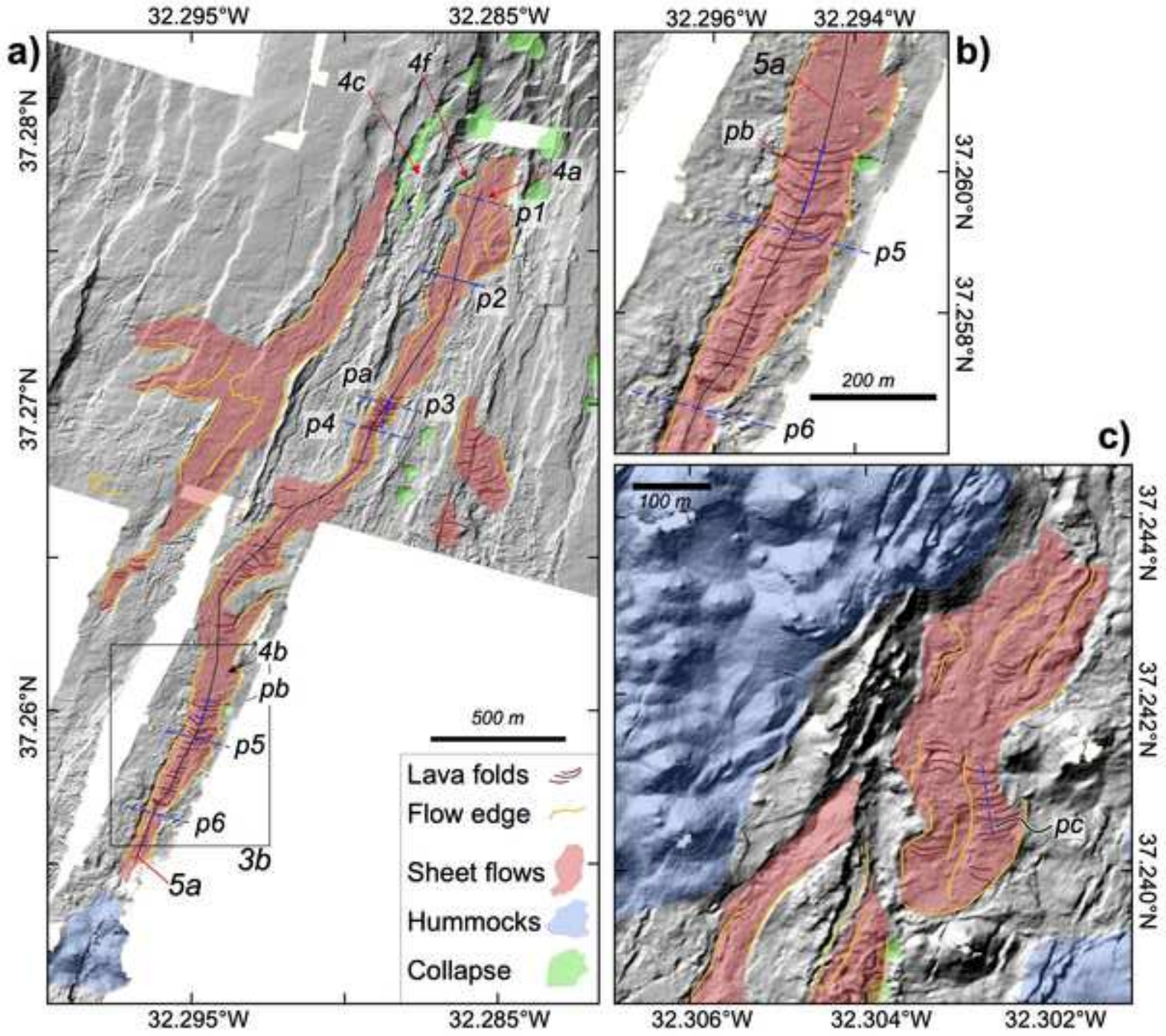

Figure4

Click here to access/download;Figure;Fig4.jpg

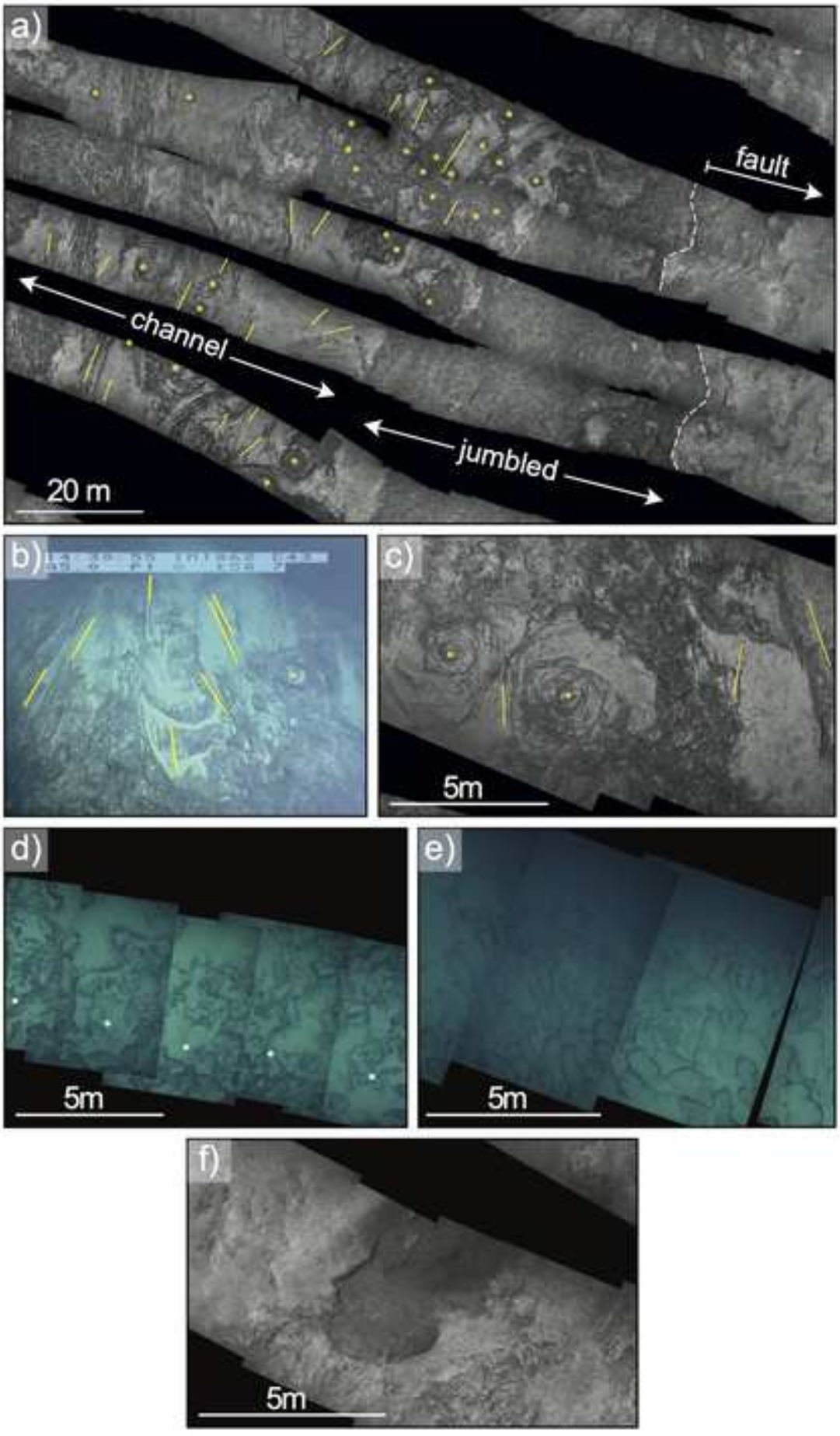

Figure5

Click here to access/download;Figure;Fig5.jpg

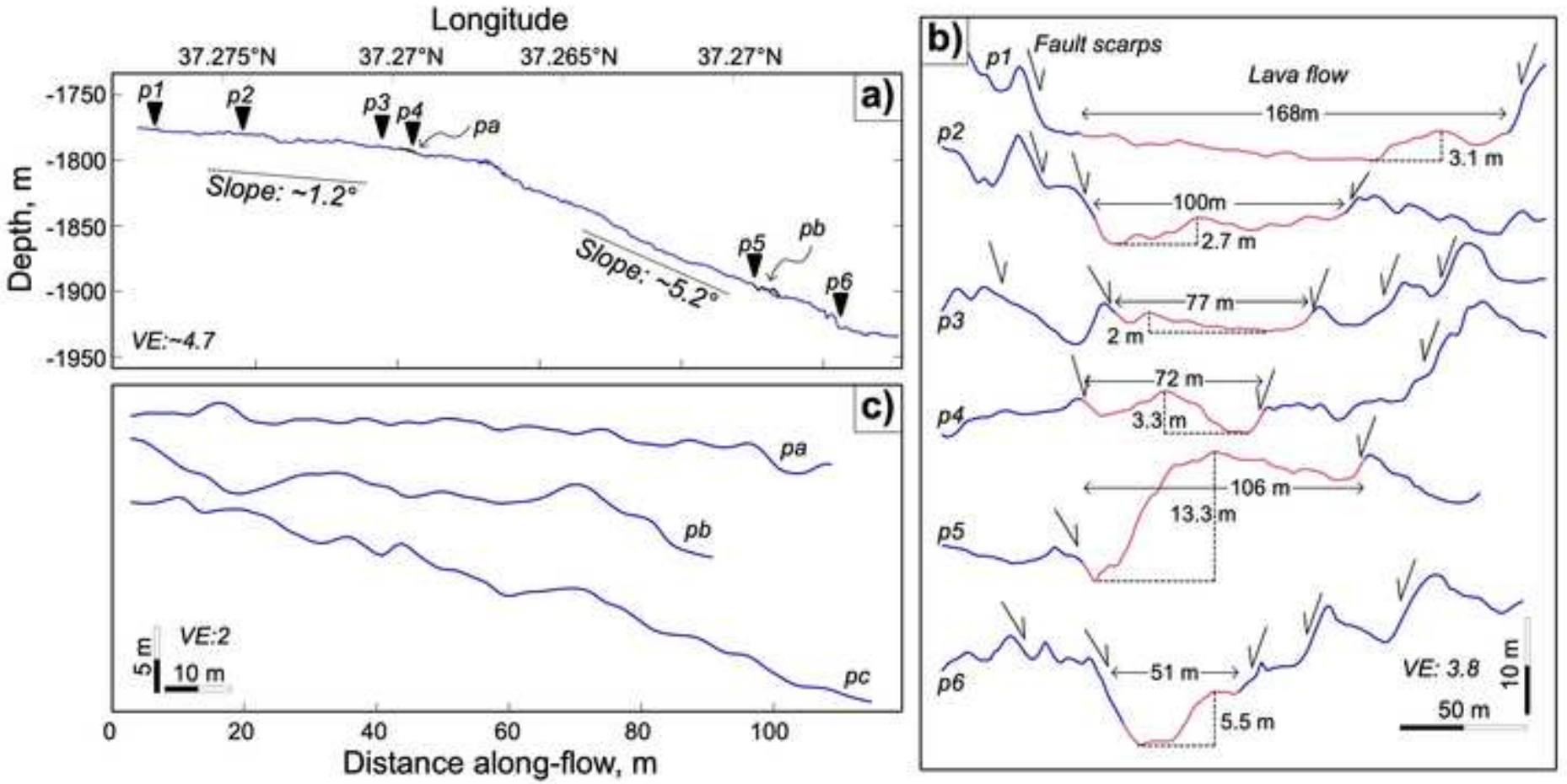

Figure6

Click here to access/download;Figure;Fig6.jpg

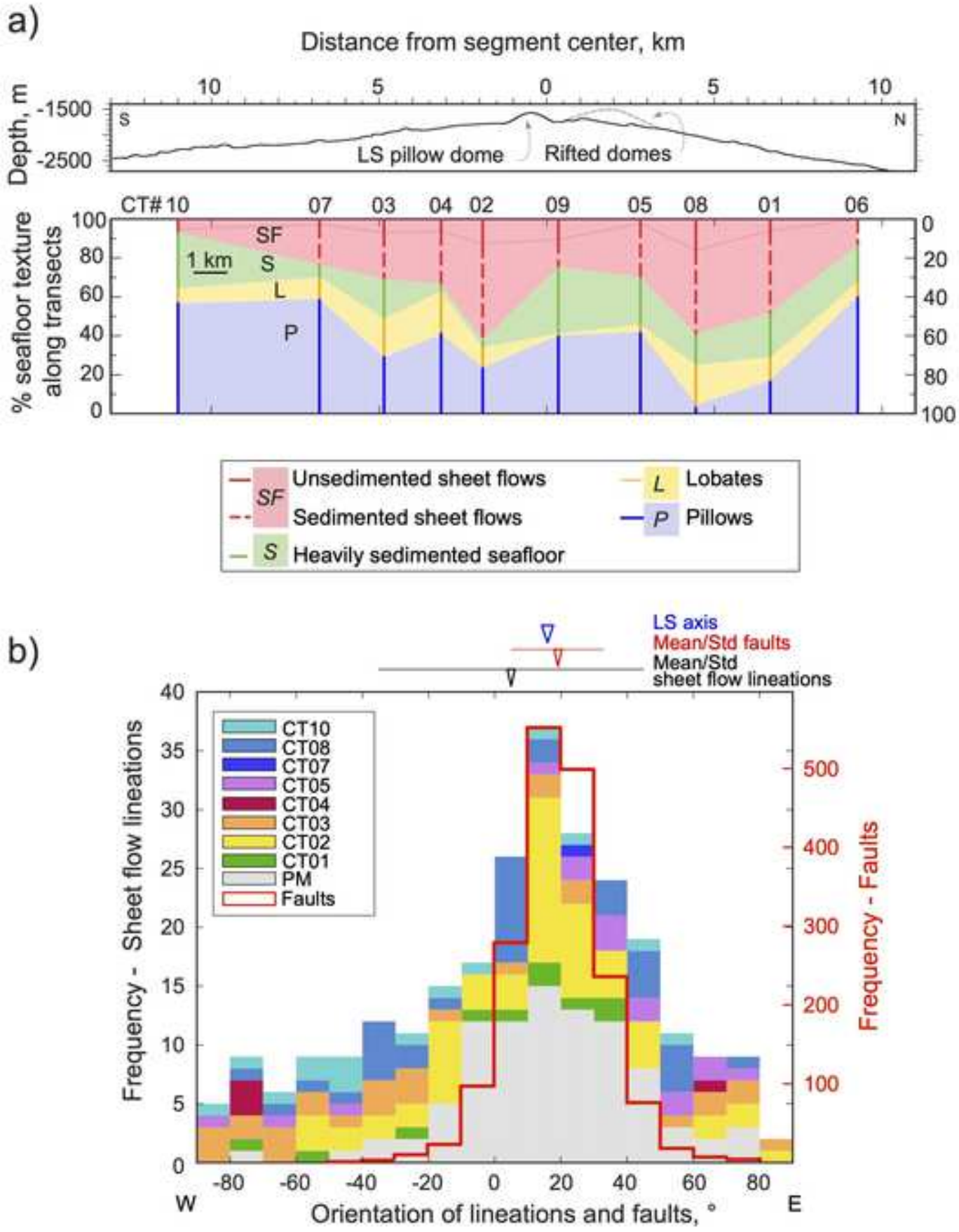

Figure7

Click here to access/download;Figure;Fig7.jpg

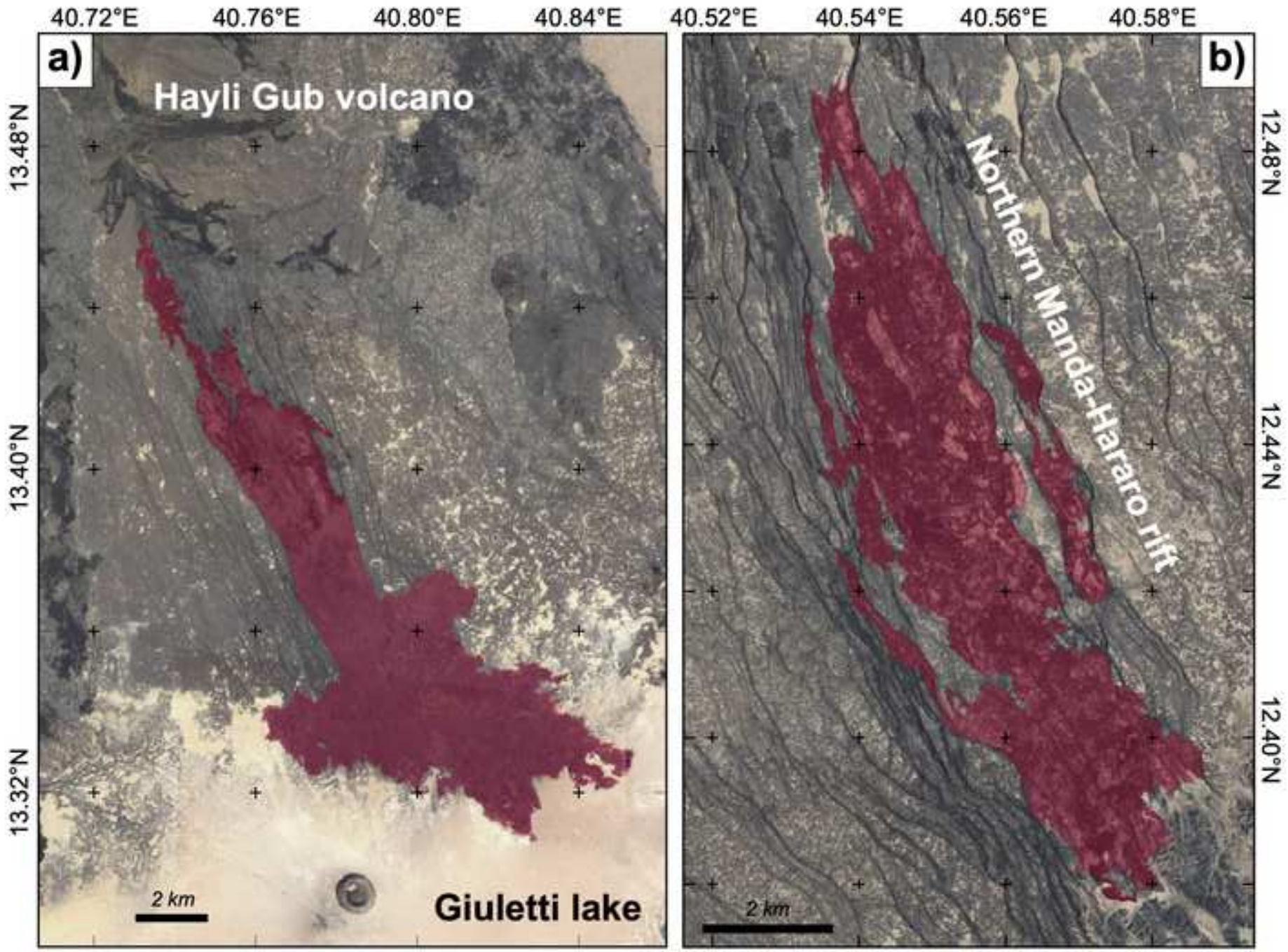

Figure8

Click here to access/download;Figure;Fig8.jpg

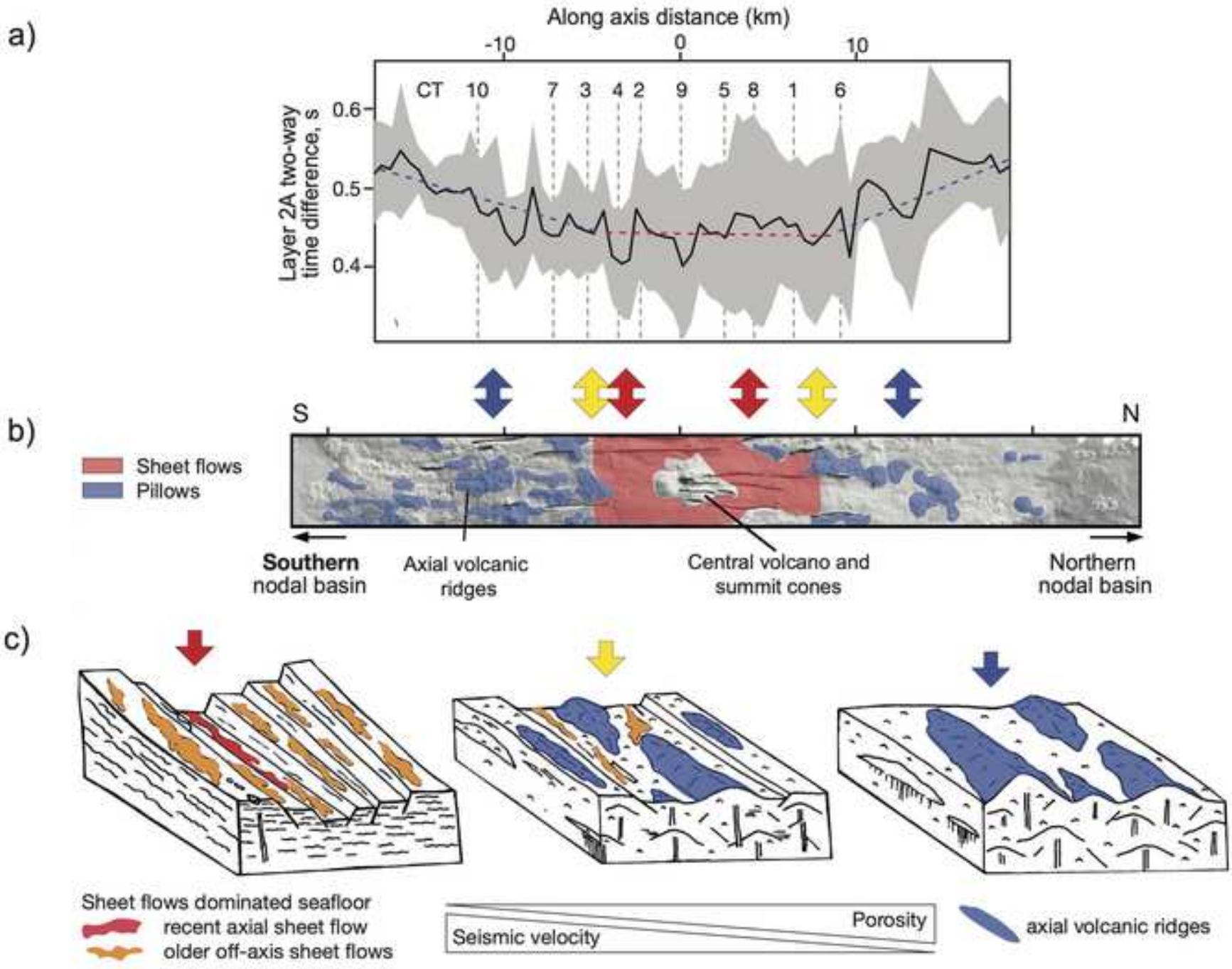

Extrusive upper crust formation at slow-spreading ridges: fault steering of lava flows and magma supply gradients

C. Gini[1,3], J. Escartín[2], M. Cannat[3] & T. Barreyre[4]

[1]Dept. of Earth Sciences, Memorial University of Newfoundland, St. John's, Canada

[2]Laboratoire de Géologie, UMR 8538, Ecole Normale Supérieure, PSL Research University, CNRS, Paris, France

[3]Université de Paris, Institut de Physique du Globe de Paris, CNRS, Paris, France

[4]Centre for Deep Sea Research, University Bergen, Bergen, Norway

Supplementary information

1. Supplementary figures

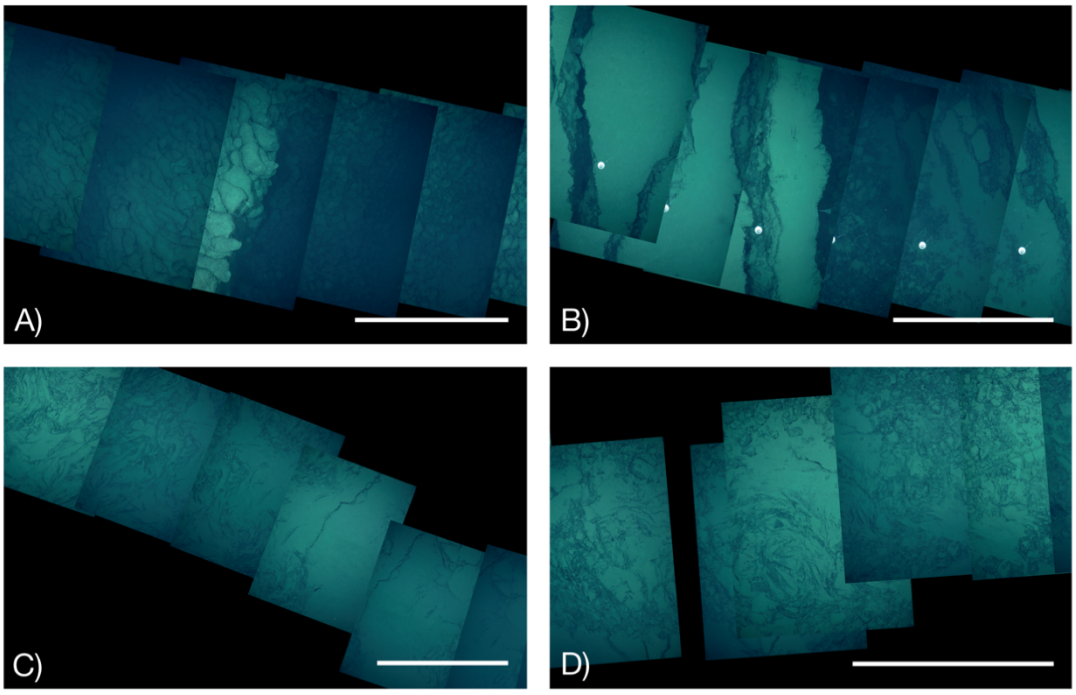

Supplementary Figure S1. *A) Fissure cross-cutting sedimented pillows (CT07, N 37.22699°N 32.29971°W). B) Fissure on sedimented seafloor (no volcanic texture visible) but showing underlying sheeted flows (CT07, 37.23124°N 32.31598°W). C) Sheeted flow and hackly margin, found off-axis and partially sedimented (CT10, 37.19636°N 32.33184°W). D) Sedimented sheet flow with lava whorls (CT10, 37.19630°N 32.33115°W). White scale bar is ~10 m.*

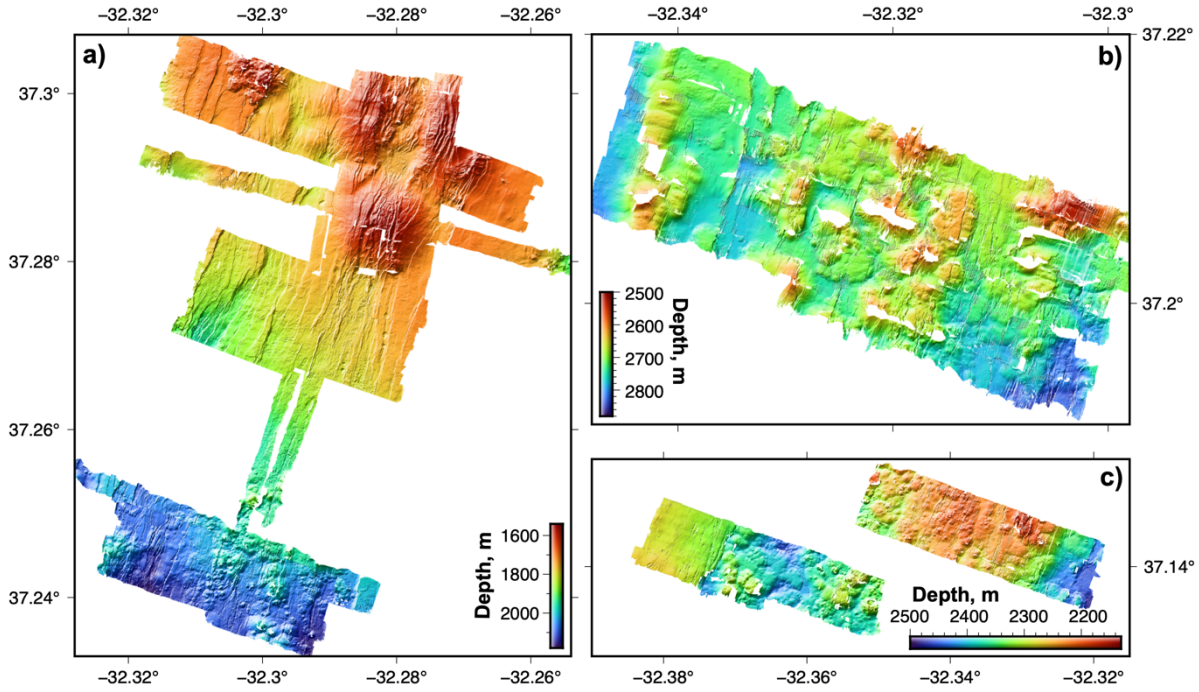

Figure S2. *Bathymetry maps acquired during ROV Victor and AUV AsterX surveys along the Lucky Strike rift valley floor (see location in Figure 1).*

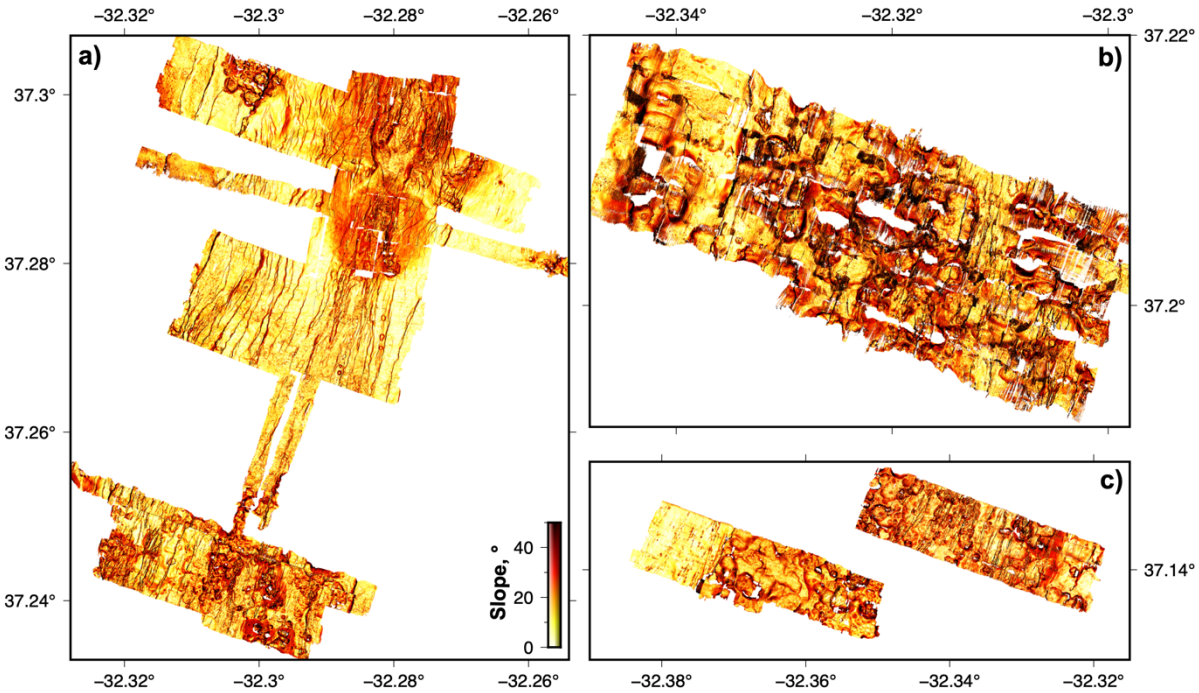

Figure S3. *Slope maps of the bathymetry shown in Figure S2, clearly revealing the differences in seafloor texture between zones dominated by lava sheet flows (north part of a) and areas dominated by hummocks and axial volcanic ridges (south of a and b, c).*

2. Data used in this study

Data were acquired over several cruises as follows:

1) During the **1996 KN145-19 "Lustre'96"** cruise (http://www.marine-geo.org/tools/entry/KN145-19) high-resolution side-scan sonar data were acquired with the DSL120 deep-towed sonar system. Black-and white vertical electronic still camera seafloor imagery was acquired with the deep-towed Argo-II camera system, in addition to observations during HOV Alvin dives.

2) During the **2006 Graviluck** cruise (doi:10.17600/6010110) vertical color seafloor digital imagery were acquired with the deep-towed TOWCAM system, while HOV Nautile acquired video imagery and recorded geological observations during dives.

Photomosaics for these camera tows were generated from vehicle navigation (layback and depth) and attitude (heading and altitude), and assuming a flat bottom. Images were not matched nor renavigated owing to limited or no overlap along track.

Photomosaics have been tiled as geotiffs, and are publicly available: doi: 10.17882/80790

3) During the **MOMARETO, MOMAR'08-Leg1 and Bathyluck cruises** in 2006, 2008 and 2009 (dois 10.17600/6030130, 10.17600/8010110 and 10.17600/9030040, respectively), near-bottom, high-resolution bathymetry data were acquired with a multibeam system mounted on the ROV VICTOR 6000 and the AUV AsterX. ROV Victor also conducted geological surveys and observations, in addition to imagery surveys, using the OTUS black and white camera vertically mounted, to obtain photomosaics of the seafloor in 2008 and 2009. Open access links to bathymetry and photomosaics are indicated below.

Data publicly available and used in this paper include microbathymetry and seafloor photomosaics:

High-resolution bathymetry. Near-bottom multibeam bathymetry data were processed post-cruise (cleaning, filtering, gridding), to obtain bathymetry grids at resolutions of either 1 m (surveys along the LS segment) or 0.50 m (survey at segment center acquired during photomosaic survey). The AUV or ROV was flown at ~70 m in average (varying between 50 to 100 m) for surveys with a resolution of 1 m per grid, and ~10 m for the surveys conducted in combination with optical imagery, and gridded at 0.5 m. Grids from different dives were manually shifted and adjusted to combine them into a single one in the central part of the segment (See Supplementary Figure S2a). Details of resulting grids and processing are partially published elsewhere (Escartín et al., 2015). Here we release the full set of near-bottom, AUV and ROV bathymetry grids: doi: 10.17882/80574

Seafloor imagery and photomosaics. Vertically acquired imagery during ROV VICTOR6000 surveys and TOWCAM tracks were processed by the Girona University for illumination corrections, renavigation, and mosaicing. VICTOR survey processing included blending of imagery to obtain seamless photomosaics that facilitate their interpretation (e.g., Barreyre et al., 2012), while imagery from tracks were photomosaiced solely on navigation and altitude information (e.g., Escartín et al., 2008), with no blending; these mosaics provide information on scale and orientation of structures, even if images are not matched and blended locally. Details on mosaicing procedures are described elsewhere (e.g., Escartín et al., 2008; Prados et al., 2012; Barreyre et al., 2012).

The 2008 photomosaic is publicly available as a series of GEOTIF tiles at doi: 10.17882/77449

The 2009 photomosaic is publicly available as a series of GEOTIF tiles at doi: 10.17882/80447

The photomosaic from the Lustre'1996 cruise (Escartín et al., 2008) is publicly available at: http://www.marine-geo.org/tools/search/Files.php?data_set_uid=6138

ROV and HOV observations. ROV and HOV dives provided geological observations throughout the study area during different dives. All imagery available to us (still images and video) was examined to extract relevant geological observations (types of lava flows, orientation of structures, sedimentation, etc.). The observations of this study complemented those reported by the different science parties in each of the cruises listed above.

Video imagery along ROV Victor and HOV Nautile tracks from the 2006, 2008 and 2009 cruises can be made available upon request to J. Escartín.

Acoustic backscatter: Acoustic backscatter data acquired with the deep-towed DSL120 sonar was used to provide a broader context to the near-bottom bathymetry data, and to extrapolate observations among survey areas, as it has a more continuous coverage. Details on sonar data acquisition and processing are given elsewhere (Scheirer et al., 2000; Humphris et el., 2002; Escartín et al., 2014), and the gridded sonar data with a resolution of 10 m are publicly available at: http://www.marine-geo.org/tools/search/DataSets.php?data_set_uids=7527,21460

Here we used this processed dataset, as well as its published tectonic interpretation (Escartín et al., 2014) for fault orientations.

Identification and quantification of seafloor textures and flow lineations. TowCam photomosaics were used for identification and classification of lava flow morphologies and sediment presence or absence, and for quantification of the resulting abundance of classes. For camera tows, the dominant seafloor texture was visually defined every 50 m along-track, identifying at the same the transitions, to define along-track segments. Each segment was attributed then a seafloor texture. Calculation of proportions along each TowCam track (Figure 6a) is then derived from the cumulative length of segments for each seafloor texture, normalized by the total length of each camera transect. No quantification of lava textures was done on the ROV OTUS photomosaics.

Where sheet flows with lineations were identified along the TowCam tracks, the most prominent structures where digitized to calculate their orientations. Due to the narrow across-track coverage of the seafloor, of approximately ~10 m, we were not able to map the full extent and limits of each flow. Hence lineations provide a flow direction locally, that we assume to be representative of the overall lava flow direction, that is dominantly along-axis (Figure 6b).

Supplementary Material References

Ballu, V., (2006) GRAVILUCK cruise, RV L'Atalante, https://doi.org/10.17600/6010110

Barreyre, T., Escartín, J., Garcia, R., Cannat, M., Mittelstaedt, E., and Prados, R., 2012, Structure, temporal evolution, and heat flux estimates from the Lucky Strike deep-sea hydrothermal field derived from seafloor image mosaics: Geochemistry, Geophysics, Geosystems, v. 13, no. 4, p. n/a-n/a, doi: 10.1029/2011GC003990.

Cannat, M., (1998) SUDACORES cruise, RV L'Atalante, https://doi.org/10.17600/98010080

Crawford, W.C., Singh, S.C., (2005) SISMOMAR cruise, RV L'Atalante, https://doi.org/10.17600/5010040

Dyment, J., (2008) MOMAR2008-LEG2 cruise, RV L'Atalante, https://doi.org/10.17600/8010140

Escartín, J., García, R., Delaunoy, O., Ferrer, J., Gracias, N., Elibol, A., Cufi, X., Neumann, L., Fornari, D.J., Humphris, S.E., Renard, J., 2008. Globally aligned photomosaic of the Lucky Strike hydrothermal vent field (Mid-Atlantic Ridge, 37°18.5′N): Release of georeferenced data, mosaic construction, and viewing software. Geochemistry, Geophys. Geosystems 9, n/a--n/a. https://doi.org/10.1029/2008GC002204

Escartín, J., (2008) MOMAR2008-LEG1 cruise, RV L'Atalante, https://doi.org/10.17600/8010110

Escartín, J., Barreyre, T., Gracias, N., Garcia, R., (2008). Lucky Strike hydrothermal field (Mid-Atlantic Ridge at ~37.25°N) - seafloor photomosaic (MOMAR08-Leg 1 cruise): 1-cm resolution black-and-white geotiffs (UTM zone 25 projection). SEANOE. https://doi.org/10.17882/77449

Escartín, J., Cannat, M., (2009) BATHYLUCK 2009 cruise, RV Pourquoi pas ? https://doi.org/10.17600/9030040

Escartín, J., Cannat, M., (2009). Bathyluck'09 Cruise (Lucky Strike). Horta-Horta (Portugal), August 31st - September 29th 2009. NO PourQuoi Pas ? - ROV Victor 6000 – AUV AsterX. https://doi.org/10.13155/47147

Escartín, J., (2009). EWAN hydrothermal site (Mid-Atlantic Ridge south of Lucky Strike): Seafloor photomosaic (black and white, VICTOR 6000, 2009). SEANOE. https://doi.org/10.17882/77405

Escartín, J., Fornari, D. and Humphris, S., (2014). DSL120 Sidescan Sonar Grids of the Lucky Strike Segment of the Mid-Atlantic Ridge from the R/V Knorr expedition KN145-19 (1996). IEDA. doi:10.1594/IEDA/321460

Escartín, J., Barreyre, T., Cannat, M., Garcia, R., Gracias, N., Deschamps, A., Salocchi, A., Sarradin, P.-M., Ballu, V., 2015. Hydrothermal activity along the slow-spreading Lucky Strike ridge segment (Mid-Atlantic Ridge): Distribution, heatflux, and geological controls. Earth Planet. Sci. Lett. 431, 173–185. https://doi.org/10.1016/j.epsl.2015.09.025

Escartín, J., Cannat, M., Deschamps, A., (2021). Microbathymetry from AUV and ROV Surveys (MOMARETO'06, MOMAR'08-Leg1 and BATHYLUCK'09 cruises) along the Lucky Strike ridge segment (Mid Atlantic Ridge). SEANOE. https://doi.org/10.17882/80574

Humphris, S.E., Fornari, D.J., Scheirer, D.S., German, C.R., Parson, L.M., 2002. Geotectonic setting of hydrothermal activity on the summit of Lucky Strike Seamount (37°17′N, Mid-Atlantic Ridge). Geochemistry, Geophys. Geosystems 3, 1–25. https://doi.org/10.1029/2001GC000284

Prados, R., Garcia, R., Gracias, N., Escartín, J., Neumann, L., 2012. A novel blending technique for underwater gigamosaicing. IEEE J. Ocean. Eng. 37, 10.1109/JOE.2012.2204152.

Sarradin, P-M., Sarrazin, J., (2006) MOMARETO cruise, RV Pourquoi pas ?, https://doi.org/10.17600/6030130

Scheirer, D.S., Fornari, D.J., Humphris, S.E., Lerner, S., 2000. High-resolution seafloor mapping using the DSL-120 sonar system: Quantitative assessment of sidescan and phase-bathymetry data from the Lucky Strike segment of the Mid-Atlantic Ridge. Mar. Geophys. Res. 21, 121–142. https://doi.org/10.1023/A:1004701429848